Mesh-independent proportional method to obtain ISSF and singularity index at the interface corner of three-dimensional dissimilar structures

Tatsujiro Miyazaki [a,*], Hibiki Fukuda [b], Nao-Aki Noda [c,*]

[a] *Mechanical Engineering Program, School of Engineering, Faculty of Engineering, University of the Ryukyus, 1 Senbaru, Nishihara-cho, Nakagami-gun, Okinawa 903-0213, Japan*
[b] *Department of Engineering, Graduate School of Engineering and Science, University of the Ryukyus, Nishihara-cho, Nakagami-gun, Okinawa 903-0213, Japan*
[c] *Department of Mechanical Engineering, Graduate School of Engineering, Kyushu Institute of Technology, 1-1 Sensui-cho, Tobata-ku, Kitakyushu-shi, Fukuoka 804-8550, Japan*

ARTICLE INFO

ABSTRACT

An efficient analysis method is proposed for the intensity of singular stress field (ISSF) as well as the singularity index (SI) at the interface corner of three dimensional (3D) bonded joints by using the finite element method (FEM). By varying the minimum mesh size e_{min}, the FEM stresses σ_{FEM} obtained from the FEM are investigated around the corner singular point. Then, mesh-independent expressions such as $\sigma_{FEM}(r) \cdot (e_{min})^{1-\lambda} = \text{const.}$ are derived for ISSF and SI based on the proportional stress fields in prismatic joints having similar FEM mesh pattern. Previously analyzed results coincide with the present mesh-independent results to the three digits for ISSF and SI in 3D corners. The experimental results show that the critical singular stress distributions causing debonding are almost identical at the interface corner and at the interface edge independent of the adhesive thickness. This is confirmed for the ABA joint denoting the 3D prismatic butt joints whose similar adherends A are bonded by resin B. Under a constant load, the ABC joint whose dissimilar adherends A and C are bonded by resin B has larger ISSF than the ABA joints. This ISSF difference increases with decreasing the adhesive thickness h, and this ISSF difference is more remarkable at the interface corner than at the interface edge. The debonding failure criterion is discussed by using the previous experiment conducted for ABA-, ABC-butt joints and ABA-, ABC- three step lap joints. It is found that the adhesive strength of the ABC joint can be expressed as a constant critical ISSF at the interface corner and the constant value coincides with the value of the 3D ABA joints. Those new findings show that the proposed 3D mesh-independent proportional method is especially useful for evaluating the debonding strength of the adhesive ABC joints.

1. Introduction

Recently, multi-material design has been introduced to automobiles [1–4], aircrafts [5], railway structures [6,7], and marine structures [8] to improve fuel efficiency and reduce greenhouse gas. Engineers and manufacturers are strongly interested in adhesive

---

Nomenclature

D	Depth
E	Young's modulus
e_{min}	Minimum element size
$e_0^{2D}, e_0^{2D*}, e_0^{edge}, e_0^{cor}$	Element size
$F_{\sigma,h}$	ISSF normalized by h
$F_{\sigma,W}$	ISSF normalized by W
G	Shear modulus
h	Adhesive thickness
$K_\sigma, K_\sigma^{2D}, K_\sigma^{cor}, K_\sigma^{edge}$	ISSF
$K_{\sigma c}^{2D}, K_{\sigma c}^{cor}, K_{\sigma c}^{edge}$	Critical ISSF at debonding
L	Length
M_c	Critical bending moment when debonding failure occurs
(r, θ)	Polar coordinate system
(r, θ, φ)	Spherical coordinate system
W	Width
$(x, y), (x, y, z)$	Cartesian coordinate system
α, β	Dunduns' parameters
$\lambda, \lambda_{2D}, \lambda_{cor}, \lambda_{edge}$	Singularity index
ν	Poisson's ratio
σ_c	Critical remote tensile stress when debonding failure occurs
σ_y^∞	Uniform applied stress
$\sigma_y^{2D}(r, \theta)$	Real stress at a point (r, θ) in a 2D joint
$\sigma_y^{cor}(r, \theta, \varphi), \sigma_y^{edge}(r, \theta, \varphi)$	Real stress at a point (r, θ, φ) in a 3D joint
$\sigma_y^{2D}(r)$	Real stress at a distance r on the interface $\theta = 90°$ which equals $\sigma_y^{2D}(r, \theta = \pi/2)$
$\sigma_y^{cor}(r)$	Real stress at a distance r and an angle $\varphi = 45°$ on the interface $\theta = 90°$ which equals $\sigma_y^{cor}(r, \theta = \pi/2, \varphi = \pi/4)$
$\sigma_y^{edge}(r)$	Real stress at a distance r and an angle $\varphi = 90°$ on the interface $\theta = 90°$ which equals $\sigma_y^{edge}(r, \theta = \pi/2, \varphi = \pi/2)$
$\sigma_y^{edge}(r)\|_{\varphi=\pi/4}$	Real stress at a distance r and an angle $\varphi = 45°$ on the interface $\theta = 90°$ which equals $\sigma_y^{edge}(r, \theta = \pi/2, \varphi = \pi/4)$
$\sigma_{y,FEM}^{cor}(r)$	FEM stress at a distance r and an angle $\varphi = 45°$ on the interface $\theta = 90°$
$\sigma_{y,FEM}^{edge}(r)$	FEM stress at a distance r and an angle $\varphi = 90°$ on the interface $\theta = 90°$
$\sigma_{y,FEM}^{edge}(r)\|_{\varphi=\pi/4}$	FEM stress at a distance r and an angle $\varphi = 45°$ on the interface $\theta = 90°$

Abbreviations

2D	Two dimensional
3D	Three dimensional
BJ	Butt joint
FEM	Finite element method
ISSF	Intensity of singular stress field
TSLJ	Three-step lap joint

Subscripts and superscripts

2D	Interface edge in the 2D model
cor	Interface corner in the 3D model
edge	Interface edge in the 3D model
*	Reference model [For example, $e_0^{2D*}, \sigma_{y,FEM}^{2D*}(r)$]

bonding by which dissimilar materials can be joined conveniently. In addition, compared with welding, bolts, screw and rivet, the adhesive bonding offers several advantages: high fatigue resistance, weight reduction, high sealability, and high productivity and soon [9,10]. However, there is a serious problem that the singular stress occurs at an interface edge by the mismatch of the deformation between the adhesive and adherend and causes the debonding failure by the lower load than expected [10]. The evaluation method for debonding strength is required to prevent joining member and component from debonding failure.

There are several approaches to the debonding strength evaluation: continuum mechanics, fracture mechanics, cohesive zone model (CZM) and so on [11,12]. Continuum mechanics is the traditional and simple approach. Since stress and strain can be evaluated sufficiently by standard commercial finite element method (FEM), the approach can be applied widely. The joining member and
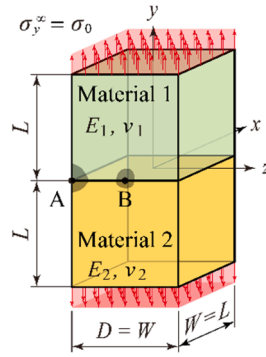
(a) 3D AB joint representing dissimilar materials where Point A represents the corner singular point and Point B represents the edge singular point.
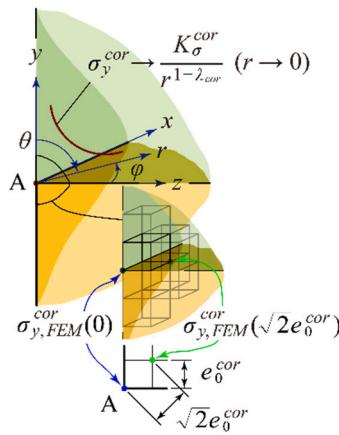
(b) Local spherical coordinate (r, θ, φ) to express corner singular stress at Point A by cubic element dimension e_0^{cor}. Note that $\sigma_y^{cor}(r, \theta = \pi/2, \varphi = \pi/4) = \sigma_y^{cor}(r)$ is always considered.
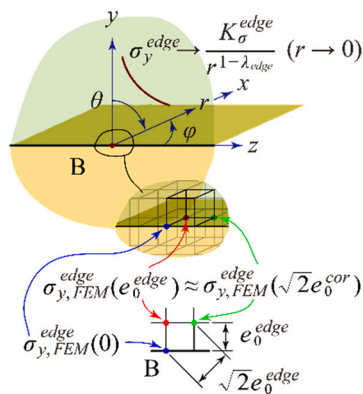
(c) Local spherical coordinate (r, θ, φ) to express corner singular stress at Point B by cubic element dimension e_0^{edge}. Here, $\sigma_y^{edge}(r, \theta = \pi/2, \varphi = \pi/2) = \sigma_y^{edge}(r)$ is mainly considered but also $\sigma_y^{edge}(r, \theta = \pi/2, \varphi = \pi/4) = \sigma_y^{edge}(r)|_{\varphi = \pi/4}$ to be compared with $\sigma_y^{cor}(r, \theta = \pi/2, \varphi = \pi/4)$.

Fig. 1. Schematic illustration for 3D AB joint consisting of cubic elements whose dimensions are e^{cor} and e^{edge} (Fig. 1 shows a butt joint named AB joint in this paper, A = Material 1, B = Material B).

component have the stress singularity at the interface edge. Although the debonding initiation site may be assumed to be the interface edge, the stress there cannot be evaluated accurately by FEM because of the stress singularity. Therefore, the continuous mechanics approach cannot be used in the debonding strength evaluation easily. The conventional fracture mechanics approach [11,12] was effectively used to evaluate the strength of structures with cracks and reported that the adhesive joint strength can be evaluated. However, usually after debonding occurs the stress intensity factor can be used and before the debonding the standard fracture mechanics approach cannot be applied to all adhesive structures unconditionally.

The CZM [11,12] is energetically studied by researchers and engineers, and most often used. In this approach, the cohesive elements have to be inserted along the crack path in advance. Since the debonding occurs at the interface edge and grows along the interface, the cohesive elements can be inserted efficiently, and the computational resource is reduced. Moreover, the simulation accuracy can be improved by implementing the XFEM and the damage mechanics. The traction-separation law plays an important role in realizing the debonding phenomena controlling the simulation accuracy significantly. Since the CZM is incorporated in commercial FEM code and some types of the laws are proposed, the users can perform various simulations and visualize failure processes. However, the users must perform some experiments to determine the parameters used in the law. Therefore, although the CZM approach suits the debonding failure simulation efficiently, it forces time-consuming work and cannot offer the debonding strength easily and conveniently.

The singular stress fields appearing at the interface edge and the interface corner cause the debonding failure. When the local polar coordinate system (r, θ) is set at the interface edge in the 2D dissimilar joint (see Fig. 1 and Fig. 2), the singular stress along the interface, $\sigma_{ij}(r, \theta)\big|_{\theta=\pi/2}$, can be expressed in the following equation [13–17].

(a) 2D AB joint representing dissimilar materials with square element where Point C represents the edge singular point.

(b) Local polar coordinate (r, θ) to express edge singular stress at Point C by square element whose dimension is e_0^{2D}.

Fig. 2. Schematic illustration for 2D AB joint consisting of square elements whose dimensions are e_0^{edge} (Fig. 2 shows a butt joint named AB joint in this paper, A = Material 1, B = Material 2).

$$\sigma_{ij}(r,\theta)\,|_{\theta=\frac{\pi}{2}} \to \frac{K_{\sigma_{ij}}}{r^{1-\lambda}} = \frac{K}{r^{1-\lambda}}f_{\sigma_{ij}}(\theta)\,\Big|_{\theta=\frac{\pi}{2}} \ (r\to 0), \ K_{\sigma_{ij}} = \lim_{r\to 0}r^{1-\lambda}\sigma_{ij}\left(r,\theta=\frac{\pi}{2}\right) \tag{1a}$$

Here, λ is a singularity index, $K_{\sigma_{ij}}$ is an intensity of singular stress field (ISSF), $f_{\sigma_{ij}}$ is a characteristic angular function of θ, and K is a constant. In this paper and in authors' previous papers [18,19], to express the intensity of singular stress field, the term "ISSF" has been used in a straightforward manner (see Appendix A). The ISSF at $\theta = 90°$ is essential because in the adhesive joints debonding always starts from the interface edge or interface corner and grows along the interface. In this paper, therefore, as shown in Eqs. (1a) and (1b), the ISSF at $\theta = 90°$ is considered. Since debonding in the adhesive joints starts from the interface edge or the interface corner and grows along the interface, the singular stress along the interface $\theta = 90°$ is significantly important. In this paper, as shown in Eqs. (1a) and (1b), the ISSF when $\theta = 90°$ is considered.

Also, when the local spherical coordinate system (r, θ, φ) is set at the interface corner in the 3D dissimilar joint (see Fig. 1 and Fig. 2), as well as the 2D dissimilar joint, the singular stress along the interface, $\sigma_{ij}(r,\theta,\varphi)\,|_{\theta=\pi/2}$, can be expressed in the following equation [20].

$$\sigma_{ij}(r,\theta,\varphi)\,|_{\theta=\frac{\pi}{2}} \to \frac{K_{\sigma_{ij}}}{r^{1-\lambda}} = \frac{K}{r^{1-\lambda}}f_{\sigma_{ij}}(\theta,\varphi)\,\Big|_{\theta=\frac{\pi}{2}} \ (r\to 0), \ K_{\sigma_{ij}} = \lim_{r\to 0}r^{1-\lambda}\sigma_{ij}\left(r,\theta=\frac{\pi}{2},\varphi\right) \tag{1b}$$

The value of λ is governed by the elastic properties of the two materials and the edge geometry independent of the far-field load geometry. When λ is smaller than 1, the material combination is called the bad pair, and the singular stress field appears. To express the singularity at the 3D corner point, the singularity exponent $p = 1 - \lambda$ has been also used in the previous papers [21–25].

In the authors' previous paper [26], a 3D bad pair condition and 3D singularity index were systematically calculated at the interface

(a) Finely meshed AB joint with minimum cubic element of edge length $e_{\min} = e_0^{cor}$.

(b) Coarsely meshed AB joint with minimum cubic element of edge length $e_{\min} = ne_0^{cor}$.

(c) Enlarged meshed AB joint by n times in joint (a) with minimum cubic element of edge length $e_{\min} = ne_0^{cor}$.
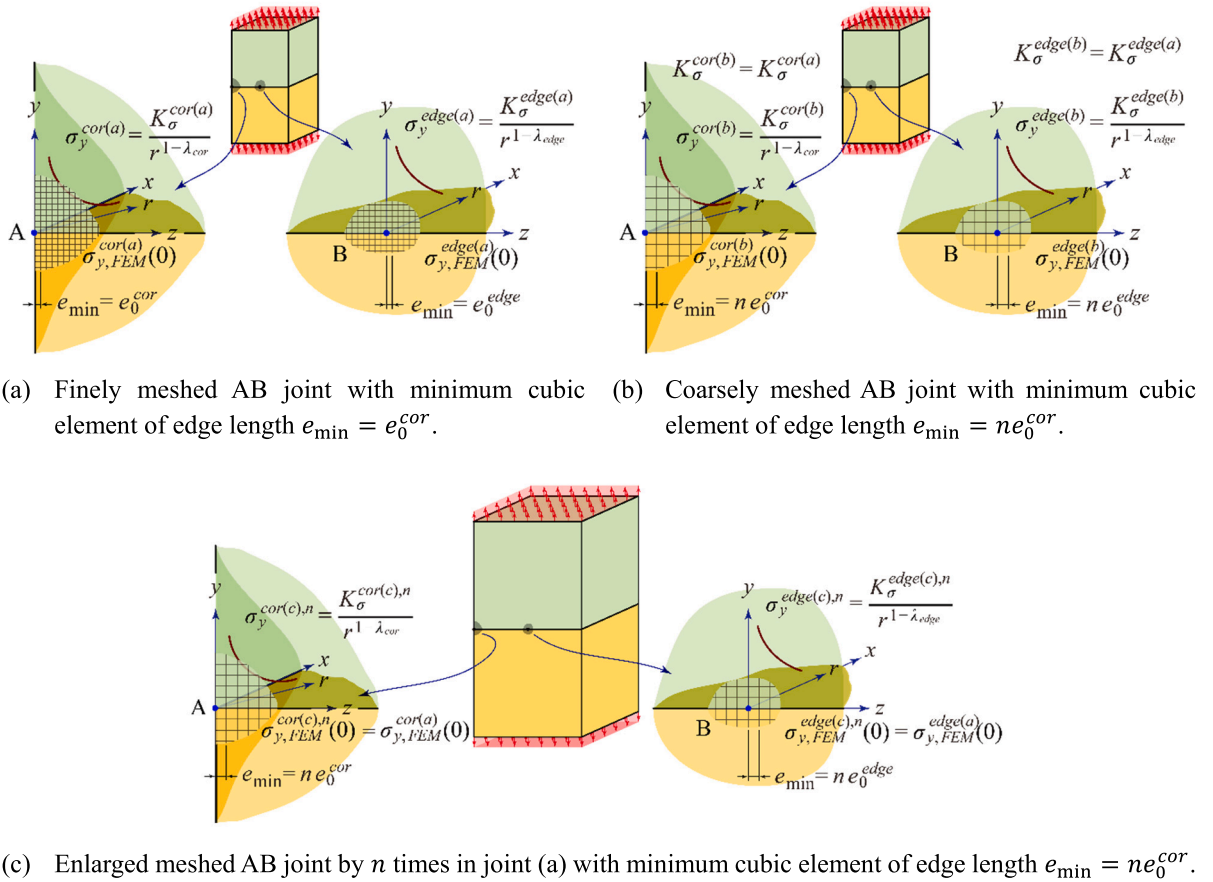
Fig. 3. Schematic illustration for the meshed AB joints (A = Material 1, B = Material 2) necessary to analyze the 3D corner singularity index. All three joints (a), (b), (c) are necessary to derive Eq. (9): $\lambda_{cor} = 1 - \ln\left\{\sigma_{y,FEM}^{cor(a)}(0)|_{e_{\min}=e_0^{cor}}/\sigma_{y,FEM}^{cor(b)}(0)|_{e_{\min}=ne_0^{cor}}\right\}/\ln n$. Two joints (a), (b) are necessary to calculate λ_{cor}. Regarding corner Point A, the singular stress $\sigma_y^{cor}(r,\theta=\pi/2,\varphi=\pi/4) = \sigma_y^{cor}(r)$ is always considered. Then, the corner ISSF can be defined as $K_\sigma^{cor}|_{\varphi=\pi/4} \equiv \lim_{r\to 0}r^{1-\lambda_{cor}}\sigma_y^{cor}(r)$. Regarding edge Point B, the singular stress $\sigma_y^{edge}(r,\theta=\pi/2,\varphi=\pi/2) = \sigma_y^{edge}(r)$ is mainly considered but sometimes $\sigma_y^{edge*}(r,\theta=\pi/2,\varphi=\pi/4) = \sigma_y^{edge}(r)|_{\varphi=\pi/4}$ is compared with $\sigma_y^{cor}(r,\theta=\pi/2,\varphi=\pi/4)$.

corner in a 3D BJ (butt joint). By comparing with a 2D bad pair condition and 2D singularity index at the interface edge in a 2D BJ, the following conclusions (A) ~ (C) were obtained. (A) The 3D bad pair condition at the 3D interface corner is slightly different from the 2D bad pair condition. Practically, the 2D bad pair condition can be practically used for 3D real material combination. (B) When the material combination satisfies both 3D and 2D bad pair conditions, the interface corner and the interface edge always have a real singularity index. Therefore, the singular stress fields at the interface corner and at the interface edge in the BJ are expressed as shown in Eqs. (1a) and (1b). (C) Values of the 3D corner singularity index at the interface corner and the 2D edge singularity index at the interface edge are different, but the difference is within 15 %.

The ISSF corresponds to the stress intensity factor (SIF) in the fracture mechanics for crack problems. The ISSFs obtained by 2D modelling were used by many researchers to predict the failure of bonded structures [17–20,27–41]. Previously, the authors reported that the adhesive strength can be expressed as a constant ISSF for the butt joint [42,43] (see Fig. A2 in Appendix A). The constant critical ISSF can be obtained by using 2D modelling for the wide range of adhesive thickness. In this way, the usefulness of the ISSF is recognized by many researchers [17–20,27–41]. However, the useful tool to evaluate the ISSF is not implemented in the commercial FEM software. Although the authors' proportional method proposed [44–47] can be used efficiently for analyzing 2D problems but it cannot be applied to 3D corner singularity problems directly. To analyze 3D corner ISSF, therefore, the eigen analysis code based on the FEM and H-integral method must be written with time-consuming and hard work. Considering these circumstances, this paper deals with efficient and convenient analysis methods for 3D corner ISSF and 3D corner singularity index.

First, in this paper, an FEM analysis method will be proposed for the interface corner in 3D bonded structures. Then, it will be shown that the 3D corner singularity index and 3D corner ISSF can be analyzed efficiently. Second, the validity and the accuracy of the proposed methods will be confirmed for the dissimilar bonded AB joint (see Fig. 1 and Fig. 2). Assume AB joint consists of A = Si and B = epoxy because this case was previously analyzed by the conventional method [48]. After confirming the validity of the present method, a prismatic ABA joint (see Fig. 8) and a prismatic ABC joint (see Fig. 14) will be analyzed. Assume they consist of the following materials and named BJ-ABA, BJ-ABC joints in this paper (BJ = Butt Joint, A = Steel, B = epoxy, C = Cu alloy). Then, the ISSFs will be analyzed by varying the adhesive thickness. Also, the effect of material combination on the ISSF will be investigated. Moreover, the suitable debonding criterion will be discussed based on the ISSF analysis and the previous experiments for the three-step lap joints (see Fig. 17) named TSLJ-ABA and TSLJ-ABC joints (TSLJ = Three-Step Lap Joint, A = Steel, B = Epoxy resin, C = Al alloy). Regarding those joints, three conditions in terms of the 2D ISSF, the 3D corner ISSF and the 3D edge ISSF will be investigated as the debonding failure criterion. Then, it will be shown that the 3D corner ISSF is more suitable than other ISSFs for 3D ABC joints.

2. Mesh-independent proportional method for 3D corner singularity index and 3D corner ISSF from FEM stress $\sigma_{FEM}(r)$

2.1. Previous studies

In this paper, an efficient analysis method will be proposed to evaluate the singularity index as well as the ISSF based on the proportional stress fields obtained by the similar FEM mesh pattern (see Fig. 3). In general, the singular stress in the adhesive joints expressed in Eqs. (1a) and (1b) can be obtained by sequentially analyzing the following (1), (2), (3):

(1) the singularity index λ,
(2) the eigenfunction $f_{\sigma_{ij}}$, and.
(3) the ISSF $K_\sigma = K \cdot f_{\sigma_{ij}}$.

In 2D dissimilar joint analyses, the singularity index λ can be obtained accurately from characteristic equation theoretically derived. The eigenfunction $f_{\sigma_{ij}}$ can be usually derived explicitly. Then, the K is often determined by a suitable method such as the proportional method [49–51] and the H-integral method numerically [48,52].

In 3D dissimilar joint analyses, (1) the singularity index λ and (2) the eigenfunction $f_{\sigma_{ij}}$ are analyzed simultaneously from the eigen analysis based on the FEM [48,53–55] because the characteristic equation and the eigenfunction have not been derived unlike the 2D dissimilar joint. Then, (3) the ISSF K_σ is determined by using a suitable numerical method such as the H-integral method. The eigen analysis is a discrete numerical analysis method and provides the eigenfunction $f_{\sigma_{ij}}$ with values. Since there are computational errors in the values of λ, $f_{\sigma_{ij}}$, and K_σ for the 3D dissimilar joint cannot be analyzed as accurately as that for the 2D dissimilar joint. It should be noted that 3D dissimilar analyses are much more time-consuming and difficult than the 2D dissimilar analyses because both the eigenvalue analysis code and the H-integral method code must be provided [48]. Furthermore, λ and $f_{\sigma_{ij}}$ in the 3D analysis can be determined using a discrete numerical analysis method, which requires a large amount of computational time and effort to ensure accuracy. In the authors' previous study, for example, a lot of time and effort was spent on calculating the 3D singularity index under arbitrary material combination to clarify the 3D corner stress singularity.

The remainder of this section is organized as follows. In Section 2.2, the analysis models of the 3D and 2D AB joints will be presented. In Section 2.3, the variation of the FEM stress is discussed by varying the minimum FEM element size. In Section 2.4, the analysis method for the 3D singularity index λ_{cor} will be proposed. In Section 2.5, the analysis method for the 3D corner ISSF K_σ^{cor} will be proposed. The present method may provide the singularity index as well as the ISSF only from the FEM stresses of the linear elements at the interface corner. Since the present method does not require time-consuming efforts and the high-performance computer, it is much more efficient and convenient than the existing methods.

2.2. Analysis modelling

Fig. 1(a) shows the 3D prismatic dissimilar bonded joint named AB joint in this study. Note that Fig. 1 (AB joint) is equivalent to Fig. 8 (ABA joint) when $h \geq W$. In ABA butt joints in Fig. 8 named BJ-ABA, if the adhesive layer thickness h is larger than or equal to the joint width W as $h \geq W$, the singular stress fields at the upper and the lower interface corners do not interfere anymore due to Saint Venant's principle. The global Cartesian coordinate system (x, y, z) is set at the center of the interface between the materials 1 and 2. It should be noted that the interface of the AB joint is expressed as $|x| \leq W/2$ and $|z| \leq W/2$ and the interface perimeter can be expressed as $|x| = W/2$ and $|z| = W/2$. The interface perimeter can be characterized by the four corners $[(x, y, z) = (-W/2, 0, -W/2)$, $(-W/2, 0, W/2), (W/2, 0, -W/2), (W/2, 0, W/2)]$ and other edge points. To represent one of the corner points, the point at $(x, y, z) = (-W/2, 0, -W/2)$ can be chosen and named the interface corner A [see Fig. 1(b)]. Instead, to represent a point on the interface edge, the point at $(x, y, z) = (-W/2, 0, 0)$ can be chosen and named the interface edge B [see Fig. 1(c)]. Then, the singularity index and the ISSF at the interface corner A and interface edge B will be evaluated by applying the proposed method.

Fig. 2(a) shows the 2D dissimilar bonded joint under the plane strain condition, which is named AB joint in this study. The global Cartesian coordinate system (x, y) is set at the end of the interface between materials 1 and 2. The point $(x, y) = (-W/2, 0)$ is denoted by the interface edge C [see Fig. 2(b)]. The ISSF at the interface edge C in the 2D AB joint can be used as the reference solution to evaluate the ISSF at the interface edge B in the 3D AB joint.

The ISSF is useful for evaluating adhesive strength. If the debonding initiates from the interface edge B, it may grow in the normal direction $\varphi = 90°$ symmetrically along the interface $\theta = 90°$. In this study, therefore, the 3D edge ISSF is defined from the singular stress analyzed on the line $\varphi = 90°$ and $\theta = 90°$ (see Fig. 1 (c)). Similarly, if the debonding initiates from the interface corner, it may grow in the bisector direction $\varphi = 45°$ symmetrically along the interface $\theta = 90°$. In this study, therefore, the 3D corner ISSF is defined from the singular stress analyzed on the line $\varphi = 45°$ and $\theta = 90°$ [see Fig. 1 (b)].

2.3. Variation of FEM stress $\sigma_{FEM}(r)|_{e_{min}}$ by varying minimum FEM mesh e_{min}

In the authors' previous paper [26], a 3D bad pair condition and 3D singularity index were discussed at the interface corner A in Fig. 1(b) and compared with a 2D bad pair condition and 2D singularity index at the interface edge C in Fig. 2 (b), which is equivalent to at the edge B in Fig. 1(c). As shown in the main conclusion indicated in Appendix A, the 3D bad pair condition at the 3D interface corner A is nearly the same but slightly different from the 2D bad pair condition at the 2D interface edge B and the 2D interface edge C. When a material combination satisfies the 3D bad pair condition indicated in Eq. (B1) in Appendix B, a singular stress field appears at the interface corner A in Fig. 1(b) as shown in Eq. (1b) [20]. When the material combination satisfies the 2D bad pair conditions indicated in Eq. (B2) in Appendix B, the singular stress field appears along the interface edge in Fig. 2(b) as shown in Eq. (1a) [20]. Under some specific material combinations, the 3D stress singularity appears at the interface corner without 2D stress singularity along the interface edge. However, since such special material combination exists in very limited regions, the 2D bad pair condition $\alpha(\alpha - 2\beta) > 0$ can be used conveniently for evaluating the 3D adhesive strength in real material combination in most cases. Here, (α, β) are Dundurs' parameter and defined as follows [56].

$$\alpha = \frac{G_1(\kappa_2 + 1) - G_2(\kappa_1 + 1)}{G_1(\kappa_2 + 1) + G_2(\kappa_1 + 1)}, \quad \beta = \frac{G_1(\kappa_2 - 1) - G_2(\kappa_1 - 1)}{G_1(\kappa_2 + 1) + G_2(\kappa_1 + 1)}, \quad \kappa_m = 4 - 3\nu_m \quad (m = 1, \, 2) \tag{2}$$

In Eq. (2), the subscripts denote Materials 1 and 2, G_m ($m = 1, 2$) is the shear elastic modulus and ν_m is Poisson's ratio for material $m = 1, 2$. When the material combination satisfies the 3D bad pair condition and the 2D bad pair condition, the interface corner and the interface edge always have a real singularity index. Therefore, the singular stress fields are expressed as shown in Eq. (1b) at the interface corner and at the interface edge. The 3D corner singularity index λ_{cor} at the interface corner A is different from the 2D edge singularity index λ_{edge} at the interface edge B. Under fixed (α, β), the λ_{cor} varies about 12 % for the largest case by varying the material combination. Values of λ_{cor} and λ_{2D} are not very different under fixed (α, β). Under the well-known 2D bad pair condition $\alpha(\alpha - 2\beta) > 0$, the ratio $\lambda_{cor}/\lambda_{2D}$ is in the range of $0.85 \leq \lambda_{cor}/\lambda_{2D} < 1$ or $\lambda_{cor}/\lambda_{2D} \simeq 1$. The λ_{edge} coincides with the λ_{2D} at the interface edge C in Fig. 2(b) as $\lambda_{edge} = \lambda_{2D}$; and therefore, the λ_{edge} can be determined by solving the following Bogy's characteristic equation [57,58].

$$\left[\sin^2\left(\frac{\pi}{2}\lambda\right) - \lambda^2\right]^2 \beta^2 + 2\lambda^2 \left[\sin^2\left(\frac{\pi}{2}\lambda\right) - \lambda^2\right] \alpha\beta + \lambda^2(\lambda^2 - 1)\alpha^2 + \frac{\sin^2(\pi\lambda)}{4} = 0 \tag{3}$$

Different from 2D analyses, the 3D singularity index λ_{cor} is determined by discrete numerical analysis methods [53–55]. These methods are time-consuming and labor-intensive, but this is unavoidable. In this section, therefore, an efficient and conventional method is proposed to evaluate the 3D singularity index λ_{cor} from the FEM stresses. Here, FEM stress [like $\sigma_{y,FEM}(r)$] is the stress obtained by FEM analysis and is distinguished from the real stress [like $\sigma_y(r)$] obtained according to the theory of elasticity. Note that the singularity index λ_{cor} at the interface corner A in Fig. 1(b) is denoted with the 3D corner singularity index, and the singularity index λ_{edge} at the interface edge B in Fig. 1(c) is denoted with the 2D edge singularity index since λ_{edge} coincides with the singularity index λ_{2D} at the interface edge C in Fig. 2(b).

Fig. 3 illustrates three models to investigate real singular stress fields $\sigma_y^{cor}(r)$, $\sigma_y^{edge}(r)$, and $\sigma_y^{edge}(r)|_{\varphi=\pi/4}$ in the 3D AB joint in Fig. 1(a). All three models consist of hexahedral elements and similar mesh patterns. The model (a) has a minimum element standard size $e_{min} = e_0^{cor}$ as shown in Fig. 3(a). Regarding the model (a), the FEM stress distribution at the interface corner A is denoted by $\sigma_{y,FEM}^{cor(a)}(r)|_{e_{min}=e_0^{cor}}$,

and the ISSF at the interface corner A is denoted by $K_\sigma^{cor(a)}$. The model (b) is as large as the model (a) but the model (b) has n times larger size $e_{\min} = ne_0^{cor}$ as shown in Fig. 3(b). Regarding the model (b), the FEM stress at the interface corner A is denoted by $\sigma_{y,FEM}^{cor(b)}(r)|_{e_{\min}=ne_0^{cor}}$, and ISSF at the interface corner A is denoted by $K_\sigma^{cor(b)}$. The model (c) is n times as large as the model (a) and divided into the regular hexahedral elements with an edge length of $e_{\min} = ne_0^{cor}$. Regarding the model (c), the FEM stress at the interface corner A is denoted by $\sigma_{y,FEM}^{cor(c),n}(r)|_{e_{\min}=ne_0^{cor}}$, and the ISSF at the interface corner A is denoted by $K_\sigma^{cor(c),n}$. Since the model (c) is equivalent to the model obtained by enlarging the model (a) including the mesh by n times, the same computational error occurs in the FEM stresses at the interface corner A and the interface edge B in the models (a) and (c). Therefore, we have $\sigma_{y,FEM}^{cor(a)}(0)|_{e_{\min}=e_0^{cor}} = \sigma_{y,FEM}^{cor(c),n}(0)|_{e_{\min}=ne_0^{cor}}$. The model (c) is an auxiliary model for deriving the evaluation formula for the λ_{cor}. When the λ_{cor} is evaluated by the present method, the FEM analyses are performed on the models (a) and (b) actually, and the present method focuses on only two FEM stresses $\sigma_{y,FEM}^{cor(a)}(0)|_{e_{\min}=e_0^{cor}}$ and $\sigma_{y,FEM}^{cor(b)}|_{e_{\min}=ne_0^{cor}}$.

Enlarged meshed AB joint in Fig. 3(c) is equivalent to the finely meshed AB joint in Fig. 3(a) since Fig. 3(c) is the enlargement of Fig. 3(a) by n times. The FEM singular stress in the y direction at the distance r_0 away from the interface corner A in the model (a) equals that at the distance nr_0 away from the interface corner A in model (c) as shown in Eq. (4a). Also, the real singular stress in the y direction at the distance r_0 away from the interface corner A in the model (a) equals that at the distance nr_0 away from the interface corner A in model (c) as shown in Eq. (4b) and Eq. (4c).

$$\sigma_{y,FEM}^{cor(a)}(r_0)|_{e_{\min}=ne_0^{cor}} = \sigma_{y,FEM}^{cor(c),n}(nr_0)|_{e_{\min}=ne_0^{cor}} \quad \text{(a-c relation 1)} \tag{4a}$$

$$\sigma_y^{cor(a)}(r_0) = \sigma_y^{cor(c),n}(nr_0) \quad \text{(a-c relation 2)} \tag{4b}$$

$$\frac{K_\sigma^{cor(a)}}{(r_0)^{1-\lambda_{cor}}} = \frac{K_\sigma^{cor(c),n}}{(nr_0)^{1-\lambda_{cor}}} \quad \text{(a-c relation 3)} \tag{4c}$$

Equation (4c) can be rewritten as follows.

$$K_\sigma^{cor(c),n} = n^{1-\lambda_{cor}} \cdot K_\sigma^{cor(a)} \quad \text{(a-c relation 4)} \tag{4d}$$

Equations (4a) − (4d) are the relation of the FEM stress and the real stress between the AB joint in Fig. 3 (a) and the AB joint in Fig. 3(c).

Next, consider the relation between the AB joint in Fig. 3(b) and the AB joint in Fig. 3(c). Since both interface corners in the AB joint (b) and in the AB joint (c) are composed of the regular hexahedral elements with the same edge length $e_{\min} = ne_0^{cor}$, the ISSF ratio can be expressed by the FEM stress ratio according to the mesh independent technique previously investigated as follows[43–45].

$$\frac{K_\sigma^{cor(c),n}}{K_\sigma^{cor(b)}} = \frac{\sigma_{y,FEM}^{cor(c),n}(0)|_{e_{\min}=ne_0^{cor}}}{\sigma_{y,FEM}^{cor(b)}(0)|_{e_{\min}=ne_0^{cor}}} \quad \text{(b-c relation 1)} \tag{5}$$

By substituting Eq. (4a) and Eq. (4d) into Eq. (5), the following equation (6a) can be obtained.

$$\frac{n^{1-\lambda_{cor}} \cdot K_\sigma^{cor(a)}}{K_\sigma^{cor(b)}} = \frac{\sigma_{y0,FEM}^{cor(a)}(0)|_{e_{\min}=e_0^{cor}}}{\sigma_{y,FEM}^{cor(b)}(0)|_{e_{\min}=ne_0^{cor}}} \quad \text{(a-b relation 1)} \tag{6a}$$

Equation (6a) can be regarded as the relation between the AB joint (a) and the AB joint (b). The ISSF ratio (= real stress ratio) can be expressed by the FEM stress ratio. Two joints have different FEM mesh but the same dimension and the same real ISSF.

$$K_\sigma^{cor(a)} = K_\sigma^{cor(b)} \quad \text{(a-b relation 2)} \tag{6b}$$

Finally, Equation (7) is derived.

$$\sigma_{y,FEM}^{cor(b)}(0)|_{e_{\min}=ne_0^{cor}} = \frac{\sigma_{y,FEM}^{cor(a)}(0)|_{e_{\min}=e_0^{cor}}}{n^{1-\lambda_{cor}}} \quad \text{(a-b relation 3)} \tag{7}$$

When $(ne_0^{cor})^{1-\lambda_{cor}}$ is multiplied by both sides of Eq. (7), the following equation is obtained.

$$\sigma_{y,FEM}^{cor(a)}(0)|_{e_{\min}=e_0^{cor}} \cdot (e_0^{cor})^{1-\lambda_{cor}} = \sigma_{y,FEM}^{cor(b)}(0)|_{e_{\min}=ne_0^{cor}} \cdot (ne_0^{cor})^{1-\lambda_{cor}} = \text{constant} \quad \text{(a-b relation 4)} \tag{8}$$

Equation (8) is important because it provides how the FEM stress $\sigma_{y,FEM}^{cor(a)}(0)|_{e_{\min}}$ varies depending on the minimum element size $e_{\min}$. Since the real stress at the interface corner goes to infinity, the FEM provides only approximate stress different from the real stress. Although the FEM stress depends on the mesh strongly, the relation between the FEM stress and the mesh had been unknown. However, when the FEM analyses are performed by changing the $e_{\min}$ using a similar mesh pattern like Fig. 3(a), (b), the FEM stress is inversely proportional to the $(e_{\min})^{1-\lambda_{cor}}$ as shown in Eq. (8). The validity of Eq. (8) is numerically confirmed in Appendix C.

2.4. Mesh-independent expression for 3D corner singularity index from FEM stress $\sigma_{FEM}(r)\mid_{e_{min}}$

Equation (8) is also useful for obtaining the singularity index λ_{cor}. Solving Eq. (8) on the λ_{cor}, the following mesh-independent formula (9) can be derived.

$$\lambda_{cor} = 1 - \frac{\ln\left\{\sigma_{y,FEM}^{cor(a)}(0)\mid_{e_{min}=e_0^{cor}} / \sigma_{y,FEM}^{cor(b)}(0)\mid_{e_{min}=ne_0^{cor}}\right\}}{\ln n} \tag{9}$$

To obtain the corner singularity index λ_{cor}, Eq. (9) is much easier and more convenient than conventional methods. The eigen analysis based on the FEM has been commonly used. The interface corner is divided into elements. The eigen equation is assembled according to the virtual work principle and solved numerically. Therefore, the method requires complex and very difficult calculations. Instead, the proposed method requires only two FEM stresses which can be obtained by changing the minimum element size e_{min} at the interface corner.

The formula (8) is quite general and can be applied for obtaining others. By replacing the corner FEM stresses $\sigma_{y,FEM}^{cor(a)}(0)\mid_{e_{min}=e_0^{cor}}$ and $\sigma_{y,FEM}^{cor(b)}(0)\mid_{e_{min}=ne_0^{cor}}$ in Eq. (9) with the edge FEM stresses $\sigma_{y,FEM}^{edge(a)}(0)\mid_{e_{min}=e_0^{edge}}$ and $\sigma_{y,FEM}^{edge(b)}(0)\mid_{e_{min}=ne_0^{edge}}$, respectively, the mesh-independent formula for evaluating the λ_{edge} can be obtained as follows.

$$\lambda_{edge} = 1 - \frac{\ln\left\{\sigma_{y,FEM}^{edge(a)}(0) / \sigma_{y,FEM}^{edge(b)}(0)\mid_{e_{min}=ne_0^{edge}}\right\}}{\ln n} \tag{10}$$

Here, $\sigma_{y,FEM}^{edge(a)}(0)\mid_{e_{min}=e_0^{edge}}$ and $\sigma_{y,FEM}^{edge(b)}(0)\mid_{e_{min}=ne_0^{edge}}$ are the FEM stresses at the interface edge B $(x,y,z) = (-W/2,0,0)$ in the finely meshed 3D AB joint model (a) and the coarsely meshed 3D AB joint model (b), respectively. The singularity index at the interface edge B, λ_{edge}, can evaluated by Eq. (10). The present method can be applied to the 2D bonded structures as well as the 3D bonded structures, and the singularity index can be obtained much more easily and conveniently than the conventional methods [48,53–55,57–60].

2.5. Mesh-independent expression for 3D corner ISSF from FEM stress $\sigma_{FEM}(r)\mid_{e_{min}}$

The authors proposed the mesh-independent technique named proportional method [49–51] useful for evaluating the 2D ISSF for the adhesive joint. The authors also reported that the method can be applied to various adhesive joints: BJ-ABA [46,48], cylindrical BJ-ABA [44], single lap joint-ABA [45,47] and so on. In this paper, an efficient mesh-independent analysis method will be proposed useful for analyzing the 3D corner ISSFs. The method for analyzing the ISSF K_σ^{cor} at the interface corner A will be described by taking an example of AB joint in Fig. 1(a). Here, as a reference solution the ISSF K_σ^{2D} at the interface edge C in Fig. 2(b) will be used.

As shown in Fig. 1(b), the local spherical coordinate (r,θ,φ) are set at the interface corner A in the 3D AB joint model, where r is the radial distance from the interface corner A, θ is the angle between the free edge which passes through the interface corner A, φ is the angle between the r axis and the interface edge which passes through the interface corner A. When $\theta = \pi/2$ and $\varphi = \pi/4$, the singular stress along r axis from the interface corner A is expressed with the singular function of r as follows [48].

$$\sigma_y^{cor}(r) \to \frac{K_\sigma^{cor}\mid_{\varphi=\frac{\pi}{4}}}{r^{1-\lambda_{cor}}}(r \to 0), \quad K_\sigma^{cor}\mid_{\varphi=\frac{\pi}{4}} \equiv \lim_{r \to 0} r^{1-\lambda_{cor}}\sigma_y^{cor}(r) \tag{11}$$

Here, $K_\sigma^{cor}\mid_{\varphi=\pi/4}$ is the ISSF defined from the singular stress along the radial line $\varphi = \pi/4$ on the interface $\theta = \pi/2$. When $\theta = \pi/2$ and $\varphi = \pi/4$, the average of the y directional stress from the interface corner A to $r = \sqrt{2}e_0^{cor}$, $\overline{\sigma}_y^{cor}$, is expressed as follows.

$$\overline{\sigma}_y^{cor} = \frac{1}{\sqrt{2}e_0^{cor}} \int_0^{\sqrt{2}e_0^{cor}} \sigma_y^{cor}(r)dr = \frac{1}{\sqrt{2}e_0^{cor}} \int_0^{\sqrt{2}e_0^{cor}} \frac{K_\sigma^{cor}\mid_{\varphi=\frac{\pi}{4}}}{r^{1-\lambda_{cor}}} dr = \frac{K_\sigma^{cor}\mid_{\varphi=\frac{\pi}{4}}}{\lambda_{cor}}\left(\sqrt{2}\,e_0^{cor}\right)^{\lambda_{cor}-1} \tag{12}$$

The local spherical coordinates (r,θ,φ) are set at the interface edge B in the 3D AB joint, where r is the radial distance from the interface edge B, θ is the angle between r axis and the line which is parallel to x axis and passes through the interface edge B, φ is the angle between the interface edge which passes through the interface edge B and r axis. When $\theta = \pi/2$ and $\varphi = \pi/4$, the y directional singular stress along r axis from the interface edge B is expressed with the singular function of r as follows.

$$\sigma_y^{edge}(r)\Big|_{\varphi=\frac{\pi}{4}} \to \frac{K_\sigma^{edge}\mid_{\varphi=\frac{\pi}{4}}}{r^{1-\lambda_{edge}}}(r \to 0), K_\sigma^{edge}\Big|_{\varphi=\frac{\pi}{4}} \equiv \lim_{r \to 0} r^{1-\lambda_{cor}}\sigma_y^{edge}(r) \tag{13}$$

Here, $K_\sigma^{edge}\mid_{\varphi=\pi/4}$ is the ISSF defined from the singular stress along the radial line $\varphi = \pi/4$ on the interface $= \pi/2$. When $\theta = \pi/2$ and $\varphi = \pi/4$, the average of the y directional stress from the interface edge B to $r = \sqrt{2}e_0^{cor}$, $\overline{\sigma}_y^{edge}$, is expressed as follow.

$$\overline{\sigma}_y^{edge} = \frac{1}{\sqrt{2}e_0^{edge}} \int_0^{\sqrt{2}e_0^{edge}} \sigma_y^{edge}(r)dr = \frac{K_\sigma^{edge}\mid_{\varphi=\frac{\pi}{4}}}{\lambda_{edge}}\left(\sqrt{2}\,e_0^{edge}\right)^{\lambda_{edge}-1} \tag{14}$$

When the element at the interface corner A is the same shape as that at the interface edge B, the y directional FEM stress in the element at the interface corner A has almost the same computational error as that at the interface edge B. The computational errors in the y directional FEM stresses are canceled by taking the ratio of the $\overline{\sigma}_y^{cor}$ to the $\overline{\sigma}_y^{edge}$ as follows.

$$
\frac{\overline{\sigma}_y^{cor}}{\overline{\sigma}_y^{edge}} = \frac{\frac{K_\sigma^{cor}|_{\varphi=\frac{\pi}{4}}}{\lambda_{edge}}\left(\sqrt{2}\,e_0^{cor}\right)^{\lambda_{cor}-1}}{\frac{K_\sigma^{edge}|_{\varphi=\frac{\pi}{4}}}{\lambda_{edge}}\left(\sqrt{2}\,e_0^{edge}\right)^{\lambda_{edge}-1}} = \frac{\frac{\sigma_{y,FEM}^{cor}(0)+\sigma_{y,FEM}^{cor}(\sqrt{2}e_0^{cor})}{2}}{\frac{\sigma_{y,FEM}^{edge}(0)+\sigma_{y,FEM}^{edge}(\sqrt{2}e_0^{edge})|_{\varphi=\frac{\pi}{4}}}{2}} \tag{15}
$$

In Eq. (15), $\sigma_{y,FEM}^{cor}(0)$ is the FEM stress at the interface corner A, and $\sigma_{y,FEM}^{cor}(\sqrt{2}e_0^{cor})$ is the FEM stress at the point $(r,\theta,\varphi) = (\sqrt{2}e_0^{cor},\pi/2,\pi/4)$ on the interface which is located diagonally opposite to the interface corner A. Also, $\sigma_{y,FEM}^{edge}(0)$ is the FEM stress at the interface edge B, $\sigma_{y,FEM}^{edge}(\sqrt{2}e_0^{edge})|_{\varphi=\pi/4}$ is the FEM stress at the point $(r,\theta,\varphi) = (\sqrt{2}e_0^{edge},\pi/2,\pi/4)$ on the interface which is located diagonally opposite to the interface corner B. Equation (15) can be rewritten as follows.

$$
\frac{K_\sigma^{cor}|_{\varphi=\frac{\pi}{4}}}{K_\sigma^{edge}|_{\varphi=\frac{\pi}{4}}} = \frac{\lambda_{cor}}{\lambda_{edge}} \cdot \frac{\sigma_{y,FEM}^{cor}(0)\cdot\left(\sqrt{2}\,e_0^{cor}\right)^{1-\lambda_{cor}} + \sigma_{y,FEM}^{cor}\left(\sqrt{2}\,e_0^{cor}\right)\cdot\left(\sqrt{2}\,e_0^{cor}\right)^{1-\lambda_{cor}}}{\sigma_{y,FEM}^{edge}(0)\cdot\left(\sqrt{2}\,e_0^{edge}\right)^{1-\lambda_{edge}} + \sigma_{y,FEM}^{edge}\left(\sqrt{2}\,e_0^{cor}\right)|_{\varphi=\frac{\pi}{4}}\cdot\left(\sqrt{2}\,e_0^{edge}\right)^{1-\lambda_{edge}}} \tag{16}
$$

In Eq. (16), $\sigma_{y,FEM}^{cor}\left(\sqrt{2}\,e_0^{cor}\right)\cdot\left(\sqrt{2}\,e_0^{cor}\right)^{1-\lambda_{cor}}$ is also mesh-independent as well as $\sigma_{y,FEM}^{cor}(0)\cdot\left(\sqrt{2}\,e_0^{cor}\right)^{1-\lambda_{cor}}$ as described in Sect. 2.3. Also, $\sigma_{y,FEM}^{edge}\left(\sqrt{2}\,e_0^{cor}\right)|_{\varphi=\pi/4}\cdot\left(\sqrt{2}\,e_0^{edge}\right)^{1-\lambda_{edge}}$ is also mesh-independent as well as $\sigma_{y,FEM}^{edge}(0)\cdot\left(\sqrt{2}\,e_0^{edge}\right)^{1-\lambda_{edge}}$. Therefore, the right side of Eq. (16) is mesh-independent as described in Sect. 2.3.

As shown in Fig. 2(b), the local polar coordinate (r,θ) is set at the interface edge C in the 2D AB joint, where θ is the angle between the free edge which passes through the interface edge C and r axis. When $\theta = \pi/2$, the singular stress along r axis from the interface edge C is expressed with the following equation.

$$
\sigma_y^{2D}(r) \to \frac{K_\sigma^{2D}}{r^{1-\lambda_{2D}}} \;\; (r\to0), \;\; K_\sigma^{2D} \equiv \lim_{r\to0} r^{1-\lambda_{2D}}\sigma_y^{2D}(r) \tag{17}
$$

Here, r is the radial distance from the interface edge C, λ_{2D} is the singularity index, K_σ^{2D} is the ISSF at the interface edge C. The interface edge C in the 2D AB joint is divided into regular square elements with an edge length of e_0^{2D}. The average of the y directional stress from $r = 0$(interface edge C) to $r = e_0^{2D}$ is expressed by the following equation.

$$
\overline{\sigma}_y^{2D} = \frac{1}{e_0^{2D}}\int_0^{e_0^{2D}}\sigma_y^{2D}(r)dr = \frac{K_\sigma^{2D}}{\lambda_{2D}}\left(e_0^{2D}\right)^{\lambda_{2D}-1} \tag{18}
$$

When $\theta = \pi/2$ and $\varphi = \pi/2$, the y directional singular stress along r axis from the interface edge B is expressed with the singular function of r as follows.

$$
\sigma_y^{edge}(r)\Big|_{\varphi=\frac{\pi}{2}} \to \frac{K_\sigma^{edge}|_{\varphi=\frac{\pi}{2}}}{r^{1-\lambda_{edge}}} \;\; (r\to0), K_\sigma^{edge}\Big|_{\varphi=\frac{\pi}{2}} \equiv \lim_{r\to0} r^{1-\lambda_{cor}}\sigma_y^{edge}(r) \tag{19}
$$

Here, $K_\sigma^{edge}|_{\varphi=\pi/2}$ is the ISSF defined from the singular stress along the radial line $\varphi = \pi/2$ on the interface $\theta = \pi/2$. The average of the y directional stress from the interface edge B to $r = e_0^{edge}$ in the 3D AB joint, $\overline{\sigma}_y^{edge}$, is expressed as follows.

$$
\overline{\sigma}_y^{edge} = \frac{1}{e_0^{edge}}\int_0^{e_0^{edge}}\sigma_y^{edge}(r)dr = \frac{K_\sigma^{edge}|_{\varphi=\frac{\pi}{2}}}{\lambda_{edge}}\left(e_0^{edge}\right)^{\lambda_{edge}-1} \tag{20}
$$

The following equation is obtained by taking the ratio of the $\overline{\sigma}_y^{2D}$ to the $\overline{\sigma}_z^{edge}$.

$$
\frac{K_\sigma^{edge}|_{\varphi=\frac{\pi}{2}}}{K_\sigma^{2D}} = \frac{\lambda_{edge}}{\lambda_{2D}} \cdot \frac{\sigma_{y,FEM}^{edge}(0)\cdot\left(e_0^{edge}\right)^{1-\lambda_{edge}} + \sigma_{y,FEM}^{edge}(e_0^{edge})\cdot\left(e_0^{edge}\right)^{1-\lambda_{edge}}}{\sigma_{y,FEM}^{2D}(0)\cdot\left(e_0^{2D}\right)^{1-\lambda_{2D}} + \sigma_{y,FEM}^{2D}(e_0^{edge})\cdot\left(e_0^{2D}\right)^{1-\lambda_{2D}}} \tag{21}
$$

In Eq. (21), $\sigma_{y,FEM}^{edge}(e_0^{edge})$ is the FEM stress at the point $(r,\theta,\varphi) = (e_0^{edge},\pi/2,\pi/2)$ on the interface which is located next to the interface edge B in the x direction. Also, $\sigma_{y,FEM}^{2D}(0)$ is the FEM stress at the interface edge C, and $\sigma_{y,FEM}^{2D}(e_0^{edge})$ is the FEM stress at the point $(r,\theta) = (e_0^{2D},\pi/2)$ on the interface which is located next to the interface edge C in the x direction. Note that $\sigma_{y,FEM}^{edge}\cdot\left(e_0^{edge}\right)^{1-\lambda_{edge}}$, $\sigma_{y,FEM}^{edge}\cdot\left(e_0^{edge}\right)^{1-\lambda_{edge}}$, $\sigma_{y,FEM}^{2D}\cdot\left(e_0^{2D}\right)^{1-\lambda_{2D}}$ and $\sigma_{y,FEM}^{2D}\cdot\left(e_0^{2D}\right)^{1-\lambda_{2D}}$ are mesh independent. Therefore, the right side of Eq. (21) is independent

of the mesh.

Consider the real stress $\sigma_y^{edge}(r,\theta,\varphi)$ expressed by the local spherical coordinate (r,θ,φ) whose origin is at point B on the edge as shown in Fig. 2(c). Since the real stress $\sigma_y^{edge}(r=r_0,\theta=\pi/2,\varphi=\pi/4)$ nearly equal the real stress $\sigma_y^{edge}(r=r_0/\sqrt{2},\theta=\pi/2,\varphi=\pi/2)$, the following relation can be derived.

$$\frac{K_\sigma^{edge}\big|_{\varphi=\frac{\pi}{2}}}{\left(r_0/\sqrt{2}\right)^{1-\lambda_{edge}}} \simeq \frac{K_\sigma^{edge}\big|_{\varphi=\frac{\pi}{4}}}{(r_0)^{1-\lambda_{edge}}} \tag{22}$$

$$\left[\because \sigma_y^{edge}(r=r_0,\theta=\pi/2,\varphi=\pi/4)=\sigma_y^{edge}\left(r=r_0\big/\sqrt{2},\theta=\pi\big/2,\varphi=\pi\big/2\right)\right]$$

Therefore, the FEM stresses $\sigma_{y,FEM}^{edge}(r_0/\sqrt{2})|_{\varphi=\pi/2}$ and $\sigma_{y,FEM}^{edge}(r_0)|_{\varphi=\pi/4}$ are almost the same as shown in Eq. (23).

$$\sigma_{y,FEM}^{edge}(r_0/\sqrt{2})|_{\varphi=\frac{\pi}{2}} \simeq \sigma_{y,FEM}^{edge}(r_0)|_{\varphi=\frac{\pi}{4}} \tag{23}$$

From Eqs. (16), (21), (22) and (23), the following equation is obtained.

$$\frac{K_\sigma^{cor}\big|_{\varphi=\frac{\pi}{4}}}{K_\sigma^{2D}} = \frac{\lambda_{cor}}{\lambda_{2D}} \cdot \frac{\sigma_{y,FEM}^{cor}(0)\cdot\left(\sqrt{2}\,e_0^{cor}\right)^{1-\lambda_{cor}} + \sigma_{y,FEM}^{cor}\left(\sqrt{2}\,e_0^{cor}\right)\cdot\left(\sqrt{2}\,e_0^{cor}\right)^{1-\lambda_{cor}}}{\sigma_{y,FEM}^{2D}(0)\cdot\left(e_0^{2D}\right)^{1-\lambda_{2D}} + \sigma_{y,FEM}^{2D}(e_0^{2D})\cdot\left(e_0^{2D}\right)^{1-\lambda_{2D}}} \tag{24}$$

It may be expected that applying a finer mesh would result in more accurate stresses and ISSFs. However, the present method is independent of the mesh size providing the same accurate ISSF values. It should be noted that although the FEM stress $\sigma_{y,FEM}$ at the 3D interface corner varies depending on the mesh size e_{min}, $\sigma_{y,FEM}$ is inversely proportional to $(e_{min})^{1-\lambda}$ as shown in Eq. (8). In other words, the term "$\sigma_{y,FEM}\cdot(e_{min})^{1-\lambda}$" is mesh-independent and can be used efficiently to analyze ISSFs.

In Eq. (24), the term "$\sigma_{y,FEM}^{cor}\left(\sqrt{2}\,e_0^{cor}\right)\cdot\left(\sqrt{2}\,e_0^{cor}\right)^{1-\lambda_{cor}}$" is also mesh-independent as well as the term "$\sigma_{y,FEM}^{cor}(0)\cdot\left(\sqrt{2}\,e_0^{cor}\right)^{1-\lambda_{cor}}$" as described in Sect. 2.3. Also, the term "$\sigma_{y,FEM}^{2D}(e_0^{2D})\cdot\left(e_0^{2D}\right)^{1-\lambda_{2D}}$" is mesh-independent as well as the term "$\sigma_{y,FEM}^{2D}(0)\cdot\left(e_0^{2D}\right)^{1-\lambda_{2D}}$" as described in Sect. 2.3. Therefore, the right side of Eq. (24) is mesh independent and provides the same accurate ISSF values independent of mesh pattern.

When the 3D corner ISSF is analyzed by the H-integral method, the eigen analysis based on the FEM must be performed by setting many integration points around the interface corner. The singularity index λ and the function $f_{\sigma_{ij}}$ are obtained from the stress values, displacements and angle functions at these points. The ISSF is obtained by performing double integral numerically. Instead, the present methods require only two stress values in the unknown and reference problems by applying a similar mesh pattern without complex and difficult calculations [see Fig. 1(b) and Fig. 2(b)]. The 3D corner ISSF can be obtained by substituting the FEM stresses into Eq. (24). The present methods are much more efficient and convenient than the existing method, such as the H-integral method.

3. Validity and accuracy of the proposed mesh-independent method for the 3D corner singularity index and 3D corner ISSF of the AB joint

3.1. Several AB joints towards analyzing the 3D corner ISSF

In Section 3, the validity and accuracy of the proposed method in Sect. 2 will be confirmed by analyzing AB joint that was previously analyzed using conventional method. Table 1 shows the elastic modulus and the Poisson's ratio for the combination of Si (= Material 1) and resin (= Material 2), Dundurs' parameter (α,β), the singularity index λ_{2D} and the ISSF for the 2D AB joint in Fig. 4(a) normalized by the plate width W, $F_{\sigma,W}^{2D*} = K_\sigma^{2D*}/(\sigma_0 W^{1-\lambda_{2D}})$. Here, (α,β) are defined as Eq. (2) [56]. The 3D prismatic AB joint composed of Si (= Material 1) and resin (= Material 2) in Table 1 will be investigated since Koguchi et al. analyzed the combination previously [48]. The singularity index $\lambda_{2D} = 0.6805$ can be determined by solving Bogy's characteristic equation (3) [57,58]. Then, the dimensionless ISSF $F_{\sigma,W}^{2D*} = 0.407$ can be obtained from the previous references [61,62].

Fig. 4 illustrates 2D and 3D AB joints to confirm the validity and usefulness of the mesh-independent method for the 3D corner singularity index and the ISSF. As shown in Fig. 4(a), (b), (c) and (d), 4 models are discussed when $L/W = 1$, $W = 2$ mm and $\sigma_y^\infty = \sigma_0 = 1$ MPa. Fig. 4(a) shows a 2D AB joint which can be used as a reference problem because the analytical exact solution obtained by the

Table 1
Material properties of 2D and 3D AB joints in Fig. 4(a)-(d). Fig. 4(a) is a reference problem used as K_σ^{2D} in Eq. (24) and Fig. 4(d) is an unknown problem whose ISSF is compared with Koguchi et al[48]. Since Fig. 4(a) is used as a reference problem, Fig. 4(b), (c) are also considered as other unknown problems since they are in plane strain condition. All AB joints in Fig. 4(a)-(d) are composed of A = Si and B = epoxy resin.

Material 1 E_1[GPa]	ν_1	Material 2 E_2[GPa]	ν_2	α	β	λ_{2D}	Reference value $F_{\sigma,W}^{2D*}$ in Fig. 4(a)
166.0	0.26	2.74	0.38	0.9647	0.1844	0.6805	0.407
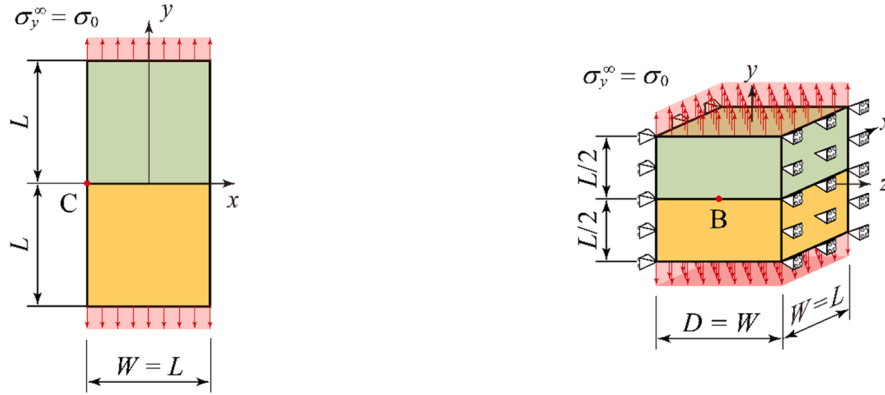
(a) 2D AB joint including plane strain condition as $\varepsilon_z = 0$ used as a reference solution since the exact solution is available under arbitrary material combination.

(b) 3D AB joint whose $z = \pm W/2$ surfaces are fixed so that $\varepsilon_z = 0$. Since Fig. 4(a) is used as a reference problem, Fig. 4(b) is considered as an unknown problem since it can be regarded as a plane strain 2D problem.
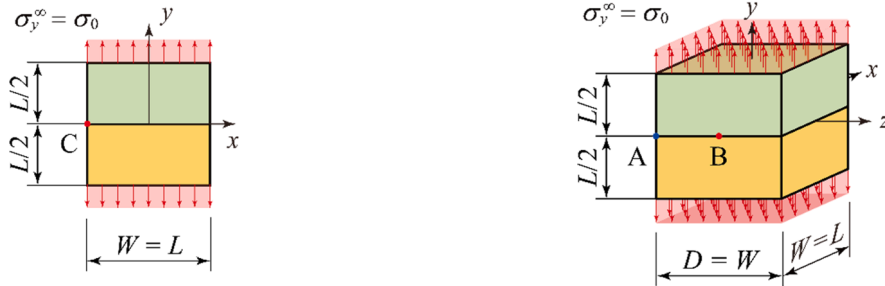
(c) 2D AB joint under plane strain condition as $\varepsilon_z = 0$. Since the 2D problem in Fig. 4(a) is used as a reference problem, Fig. 4(c) is considered as an unknown 2D plane strain problem.

(d) 3D AB joint to obtain 3D corner ISSF as the target problem to be compared with Koguchi et al[48].

Fig. 4. Several AB joints considered in this study toward analyzing the 3D corner ISSF in Fig. 4(d) to be compared with Koguchi et al [48]. Since the 2D problem in Fig. 4(a) is used as a reference problem, Fig. 4(b), (c) are also considered as other unknown problems since they can be regarded as 2D plane strain problems. All 3D AB joints in Fig. 4(a) ~ (d) are composed of A = Si and B = epoxy resin.

body force method [61,62] is available under arbitrary material combinations. Note that $L/W = 1$ in Fig. 4(a) can be regarded as when $L/W \geq 1$. Fig. 4(d) shows a target problem whose corner ISSF will be compared with the results of Koguchi et al [48] to confirm the validity of the proposed analysis method.

In this analysis, Fig. 4(b), (c) are also considered as other unknown problems. This is because Fig. 4(a) is used as the reference problem but 2D problem including plane strain condition. In Fig. 4(b), the displacement in the z-direction are fixed at $z = \pm W/2$ so that Fig. 4(b) can be regarded as 2D plane strain condition $\varepsilon_z = 0$. In this way, the accuracy and validity of the proposed method is confirmed. The length of AB joints in Fig. 4(b), (c) is set as L equal to the length of the target problem in Fig. 4(d) and half of $2L$ in the reference problem in Fig. 4(a). In Fig. 4(b), the ISSF at the interface edge B will be analyzed. In Fig. 4(d), the ISSFs at the interface corner A and the interface edge B in the 3D AB joint will be analyzed. The elastic stress analyses are performed by using the commercial FEM code MARC.

Fig. 5(a) illustrates the FEM mesh used for the reference 2D AB joint in Fig. 4(a). The same mesh pattern is also used in the 2D AB joint in Fig. 4(c). Fig. 5(b) illustrates the mesh used for the 3D AB joints in Fig. 4(b) and (d). The 8-node hexahedral element is used in the 3D AB joints in Fig. 4(b) and (d). Also, the 4-node quadrilateral element is used in the 2D AB joint in Fig. 4(a) and (c). The linear element is used in all 3D and 2D AB joints. The FEM analyses are performed on all 3D AB joints when $e_0^{cor}/(W/2) = e_0^{edge}/(W/2) = 4.360 \times 10^{-6}$ and 1.744×10^{-5} to confirm the mesh independency. Similarly, the FEM analyses are performed on all 2D AB joints under $e_0^{2D}/(W/2) = 3^{-12}$ and 3^{-9}.
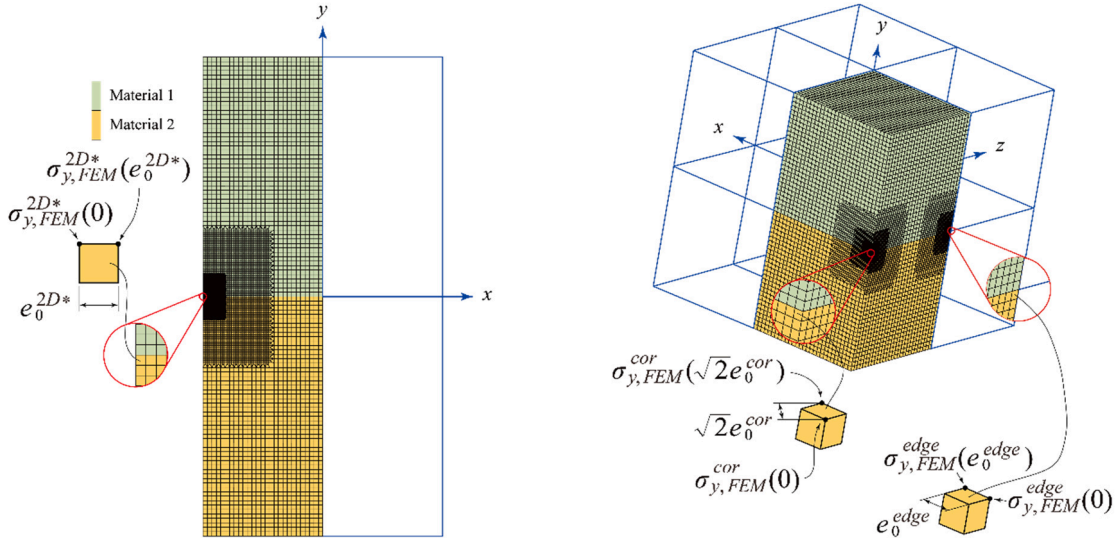
(a) FEM mesh with square element of edge length e_0^{edge} used for 2D AB joint in Figs. 4(a), (c).

(b) FEM mesh with cubic element of edge length e_0^{cor} used for 3D AB joint in Figs. 4(b), (d).

Fig. 5. FEM mesh to be used to analyze both ISSF and singularity index in Fig. 3. Fig. 5(a) shows FEM mesh in composed of square element of edge length e_0^{edge} to analyze the 2D AB joints in Fig. 4(a), (c). Fig. 5(b) shows FEM mesh composed of cubic element of edge length e_0^{cor} to analyze the 3D AB joints in Fig. 4(b), (d).

3.2. Validity and accuracy of 3D corner singularity index λ_{cor} as well as 3D edge singularity index λ_{edge} obtained by the mesh-independent method

Table 2 shows the singularity indexes λ_{edge} and λ_{cor} to confirm the accuracy of the mesh-independent method. In Table 2, the minimum cubic element size at the interface corner A, $e_0^{cor}/(W/2)$, and the minimum cubic element size at the interface edge B, $e_0^{edge}/(W/2)$, are set to be equal. In the fine mesh, they are changed in the range $e_0^{cor}/(W/2) = e_0^{edge}/(W/2) = 4.360 \times 10^{-6} \sim 2.790 \times 10^{-4}$. In the coarse mesh, the minimum cubic element size is set to be in the range $e_0^{cor}/(W/2) = e_0^{edge}/(W/2) = 1.744 \times 10^{-5} \sim 1.116 \times 10^{-3}$, which are 4 times larger than that in the fine mesh. Table 2(a) shows the results for singularity index λ_{edge} at the interface edge B in Fig. 4(b) under plane strain condition as $\varepsilon_z = 0$ to confirm the validity of the proposed method. As shown in Table 2(a), the values of λ_{edge} obtained from Eq. (9) for Fig. 4(b) are independent of the mesh size agreeing well with the results of λ_{2D}, which are obtained from the 2D characteristic equation (3) to the three digits. Since the singularity index is determined from the local geometry around the singularity point, the plane strain deformation and the external force do not affect the singularity index.

Tables 2(b), (c) examine the results for Fig. 4(d) obtained by the proposed method. As shown in Table 2(b), the values of λ_{cor} at the interface corner A obtained from Eq. (9) are independent of the mesh size agreeing well to the three digits with the results of Koguchi et al.[48], which are obtained through the eigen analysis. Since Eqs. (9) and (10) provide accurate values of λ_{cor} and λ_{edge}, the validity and usefulness of Eqs. (9) and (10) are confirmed.

As shown in Table 2(c), the values of λ_{edge} at the interface edge B in Fig. 4(d) are mesh-independent and they agree with the results in Table 2(a) as well as the results of characteristic equation (3). Comparing Table 2(a) and Table 2(c) confirms that the same singularity index λ_{edge} can be obtained from Eq. (10) as $\lambda_{edge} = 0.681$ although the FEM stresses $\sigma_{y,FEM}^{edge}(0)$ are very different in Table 2(a) and Table 2(c).

3.3. Validity and accuracy of 3D edge ISSF K_σ^{edge} obtained by the mesh-independent method

Table 3(a) shows mesh-independency of the obtained ISSF K_σ^{edge} in Fig. 4(b) where $\varepsilon_z = 0$. Table 3(b) also shows the ISSF K_σ^{2D} is mesh independent in 2D AB joint in Fig. 4(c) where $\varepsilon_z = 0$. Those results are obtained for 3D and 2D AB joints in Fig. 4(b), (c) with A = Si, B = Epoxy resin when $W = 2$ mm and $\sigma_y^\infty = 1$ MPa. In Table 3, the ISSF K_σ^{edge} values are obtained by substituting the FEM stresses $\sigma_{y,FEM}^{edge}(0)$ in Table B1 into Eq. (21). Although the fine mesh pattern and the coarse mesh pattern are combined variously, $K_\sigma^{edge} = 0.0567$ MPa $\cdot$ m$^{1-\lambda_{edge}}$ is obtained. Then, the K_σ^{edge} almost equals the K_σ^{2D}. There is about 0.43 % error between them. Fig. 6 shows the y directional FEM stress distribution by FEM analyses and the asymptotic solution with $\lambda_{edge} = 0.6809$ and $K_\sigma^{edge} = 0.0567$ MPa $\cdot$ m$^{1-\lambda_{edge}}$

Table 2

Mesh-independency of singularity index λ by varying the minimum element size $e_{\min}$ obtained by the proposed method in Eqs. (9), (10) although FEM stress σ_{FEM} varies depending on $e_{\min}$ [consider AB joints in Fig. 4(b), (d) (A = Si, B = Epoxy resin when $W = 2$ mm and $\sigma_y^\infty = \sigma_0 = 1$ MPa)]. In Table 2 (a), plane strain condition $\varepsilon_z = 0$ in Fig. 4(b) having no effect on λ is considered to confirm the validity of the proposed method. Table 3(a) referring to Fig. 4(b) where $\lambda = \lambda_{edge}$ is independent of $e_{\min} = e_0^{edge}$ but $\sigma_{y,FEM} = \sigma_{y,FEM}^{edge}(0)$ varies. Table 3(b) referring to Fig. 4(d) where $\lambda = \lambda_{cor}$ is independent of $e_{\min} = e_0^{cor}$ but $\sigma_{FEM} = \sigma_{y,FEM}^{cor}(0)$ varies. Table 3(c) referring to Fig. 4(d) where $\lambda = \lambda_{edge}$ is independent of $e_{\min} = e_0^{edge}$ but $\sigma_{FEM} = \sigma_{y,FEM}^{edge}(0)$ varies.

(a) Edge singularity index λ_{edge} obtained from FEM stress in Fig. 4(b) under plane strain condition $\varepsilon_z = 0$ using Eq. (10):

$\lambda_{edge} = 1 - \ln\left\{ \sigma_{y,FEM}^{edge(a)}(0) / \sigma_{y,FEM}^{edge(b)}(0)\big|_{e_{\min}=ne_0^{edge}} \right\} / \ln n$ in Eq. (10).

Fine mesh		Coarse mesh		λ_{edge} from Eq. (10)	λ_{2D} from Eq. (3) (conventional method)
$e_0^{edge}/(W/2)$	$\sigma_{y,FEM}^{edge}(0)$	$e_0^{edge}/(W/2)$	$\sigma_{y,FEM}^{edge}(0)$		
4.360×10^{-6}	40.63	1.744×10^{-5}	26.10	0.6809	0.6805
1.744×10^{-5}	26.10	6.975×10^{-5}	16.77	0.6807	
6.975×10^{-5}	16.77	2.790×10^{-4}	10.77	0.6809	
2.790×10^{-4}	10.77	1.116×10^{-3}	6.919	0.6807	

(b) Corner singularity index λ_{cor} obtained from FEM stress in Fig. 4(d) using Eq. (9): $\lambda_{cor} = 1 - \ln\left\{ \sigma_{y,FEM}^{cor(a)}(0)\big|_{e_{\min}=e_0^{cor}} / \sigma_{y,FEM}^{cor(b)}(0)\big|_{e_{\min}=ne_0^{cor}} \right\} / \ln n$ in Eq. (9).

Fine mesh		Coarse mesh		λ_{cor}	
$e_0^{cor}/(W/2)$	$\sigma_{y,FEM}^{cor}(0)$	$e_0^{cor}/(W/2)$	$\sigma_{y,FEM}^{cor}(0)$	From Eq. (9) (Proposed method)	Koguchi et al.[48] (Conventional method)
4.360×10^{-6}	104.9	1.744×10^{-5}	60.64	0.6050	0.605
1.744×10^{-5}	60.64	6.975×10^{-5}	35.06	0.6048	
6.975×10^{-5}	35.06	2.790×10^{-4}	20.28	0.6050	
2.790×10^{-4}	20.28	1.116×10^{-3}	11.73	0.6049	

(c) Edge singularity index λ_{edge} obtained from FEM stress in Fig. 4(d) using Eq. (10): $\lambda_{edge} = 1 - \ln\left\{ \sigma_{y,FEM}^{edge(a)}(0) / \sigma_{y,FEM}^{edge(b)}(0)\big|_{e_{\min}=ne_0^{edge}} \right\} / \ln n$ in Eq. (10).

Fine mesh		Coarse mesh		λ_{edge} from Eq. (10) (Proposed method)	λ_{2D} from Eq. (3) (Conventional method)
$e_0^{edge}/(W/2)$	$\sigma_{y,FEM}^{edge}(0)$	$e_0^{edge}/(W/2)$	$\sigma_{y,FEM}^{edge}(0)$		
4.360×10^{-6}	34.73	1.744×10^{-5}	22.32	0.6809	0.6805
1.744×10^{-5}	22.32	6.975×10^{-5}	14.34	0.6808	
6.975×10^{-5}	14.34	2.790×10^{-4}	9.212	0.6810	
2.790×10^{-4}	9.212	1.116×10^{-3}	5.918	0.6808	

Table 3

Mesh-independency of edge ISSF in Fig. 4 (b), (c) by varying minimum element size $e_{\min}$. Table 3 (a) referring to Fig. 4 (b) where FEM stress $\sigma_{y,FEM}^{edge}(0)$ and cubic element size $e_{\min} = e_0^{edge}$. Table 3(b) referring to Fig. 4(c) where FEM stress $\sigma_{y,FEM}^{edge}(0)$ and square element size $e_{\min} = e_0^{edge}$. In AB joints in Fig. 4(b), (c), $W = 2$ mm, $W = L$ and $\sigma_y^\infty = 1$ MPa.

(a) 3D AB joint under $\varepsilon_z = 0$ in Fig. 4(b).

2D reference problem in Fig. 4(a) $e_0^{2D*}/(W/2)$ [see Fig. 4(a)]	3D unknown problem in Fig. 4(b) $e_0^{edge}/(W/2)$ [see Fig. 4(b)]	K_σ^{edge} [MPa · m$^{1-\lambda_{edge}}$]
3^{-12}	4.360×10^{-6}	0.0567
3^{-12}	1.744×10^{-5}	0.0567
3^{-9}	4.360×10^{-6}	0.0567
3^{-9}	1.744×10^{-5}	0.0567

(b) 2D AB joint under $\varepsilon_z = 0$ in Fig. 4(c).

2D reference problem in Fig. 4(a) $e_0^{2D*}/(W/2)$ [see Fig. 4(a)]	3D unknown problem in Fig. 4(c) $e_0^{2D}/(W/2)$ [see Fig. 4(c)]	K_σ^{2D} [MPa · m$^{1-\lambda_{2D}}$]
3^{-12}	3^{-12}	0.0564
3^{-12}	3^{-9}	0.0564
3^{-9}	3^{-12}	0.0564
3^{-9}	3^{-9}	0.0564

obtained by the present methods. The FEM stress distribution of 3D model is in good agreement with the FEM stress distribution of 2D model well. The 3D model in Fig. 4(b) is equivalent to the 2D model in Fig. 4(c). Then, since the asymptotic solution is in good agreement with the FEM stress distributions, it can be said that the K_σ^{edge} is evaluated by the present method accurately.
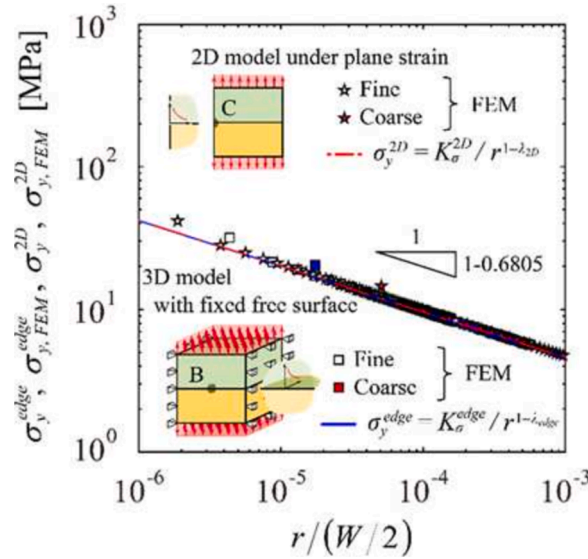
Fig. 6. Singular stress distribution at the interface edge B in Fig. 4(b) whose surfaces are fixed in the z-direction and the interface edge C in 2D AB joint under plane strain condition in Fig. 4(c) (A = Si, B = Epoxy resin, $W = 2$ mm and $\sigma_y^\infty = \sigma_0 = 1$ MPa). In Fig. 6, several plots may have some FEM errors but they can be eliminated by taking the ratio with the reference solution by applying the same FEM mesh pattern.

3.4. Validity and accuracy of 3D corner ISSF K_σ^{cor} obtained by the proposed method

Table 4 shows the 3D corner ISSF K_σ^{cor} and the 3D edge ISSF K_σ^{edge}. The 3D corner ISSF K_σ^{cor} can be obtained from Eq. (24) by substituting the value of λ_{cor} in Table 2 and the FEM stresses in Table B2 in Appendix B. The 3D edge ISSF K_σ^{edge} can be obtained from Eq. (21) by substituting the value of λ_{edge} in Table 2 and the FEM stresses in Table B2. Table 4 shows that the present results $K_\sigma^{cor} = 0.0336$ MPa $\cdot$ m$^{1-\lambda_{cor}}$ and $K_\sigma^{edge} = 0.0485$ MPa $\cdot$ m$^{1-\lambda_{edge}}$ are mesh-independent for various mesh sizes, e_0^{2D*} in Fig. 4(a) and e_0^{cor} in Fig. 4(d). Table 4(a) also indicates the results of Koguchi et al.[48] obtained by using curve fitting the BEM stresses and the H-integral method, which agree with the present results. In this analysis, as the reference solution, the results of 2D AB joint $F_{\sigma,W}^{2D*}$ in Fig. 4(a) obtained by

Table 4
Mesh-independency of the corner ISSF K_σ^{cor} and the edge ISSF K_σ^{edge} in Fig. 5(b). Consider AB joint in Fig. 4(d), A = Si, B = Epoxy resin when $W = 2$ mm and $\sigma_y^\infty = \sigma_0 = 1$ MPa.

(a) ISSF at the interface corner A, K_σ^{cor} in Fig. 4(d) obtained from the following equation [see Eq. (24)]:

$$K_\sigma^{cor}\big|_{\varphi=\frac{\pi}{4}} = \frac{\lambda_{cor}}{\lambda_{2D}} \cdot \frac{\sigma_{y,FEM}^{cor}(0) \cdot \left(\sqrt{2}\,e_0^{cor}\right)^{1-\lambda_{cor}} + \sigma_{y,FEM}^{cor}(\sqrt{2}\,e_0^{cor}) \cdot \left(\sqrt{2}\,e_0^{cor}\right)^{1-\lambda_{cor}}}{\sigma_{y,FEM}^{2D}(0) \cdot \left(e_0^{2D}\right)^{1-\lambda_{2D}} + \sigma_{y,FEM}^{2D}(e_0^{2D}) \cdot \left(e_0^{2D}\right)^{1-\lambda_{2D}}} \cdot K_\sigma^{2D}.$$

Present method			Koguchi et al. in Ref. [48]	
$e_0^{2D*}/(W/2)$	$e_0^{cor}/(W/2)$	K_σ^{cor}[MPa $\cdot$ m$^{1-\lambda_{cor}}$] in Fig. 4(d)	Curve fitting	H-integral method
3^{-12}	4.360×10^{-6}	0.0336	0.0333	0.0336
3^{-12}	1.744×10^{-5}	0.0336		
3^{-9}	4.360×10^{-6}	0.0336		
3^{-9}	1.744×10^{-5}	0.0336		

(b) ISSF at the interface edge B, K_σ^{edge} in Fig. 4(d) obtained from the following equation [see Eq. (21)]:

$$K_\sigma^{edge}\big|_{\varphi=\frac{\pi}{2}} = \frac{\lambda_{edge}}{\lambda_{2D}} \cdot \frac{\sigma_{y,FEM}^{edge}(0) \cdot \left(e_0^{edge}\right)^{1-\lambda_{edge}} + \sigma_{y,FEM}^{edge}(e_0^{edge}) \cdot \left(e_0^{edge}\right)^{1-\lambda_{edge}}}{\sigma_{y,FEM}^{2D}(0) \cdot \left(e_0^{2D}\right)^{1-\lambda_{2D}} + \sigma_{y,FEM}^{2D}(e_0^{edge}) \cdot \left(e_0^{2D}\right)^{1-\lambda_{2D}}} \cdot K_\sigma^{2D}.$$

Present method		
$e_0^{2D*}/(W/2)$	$e_0^{edge}/(W/2)$	K_σ^{edge}[MPa $\cdot$ m$^{1-\lambda_{edge}}$] in Fig. 4(d) (K_σ^{edge} [MPa $\cdot$ m$^{1-\lambda_{edge}}$] in Fig. 4(b))
3^{-12}	4.360×10^{-6}	0.0485 (0.0567)
3^{-12}	1.744×10^{-5}	0.0485 (0.0567)
3^{-9}	4.360×10^{-6}	0.0485 (0.0567)
3^{-9}	1.744×10^{-5}	0.0485 (0.0567)

the body force method is used. It can be said that the value of K_σ^{cor} from Eq. (24) is as accurately as the F_σ^{2D*}. Table 4(b) shows the results $K_\sigma^{edge} = 0.0567$ MPa · m$^{1-\lambda_{edge}}$ in Fig. 4(b), which is different from $K_\sigma^{edge} = 0.0485$ MPa · m$^{1-\lambda_{edge}}$ in Fig. 4(d). Unlike the singularity index indicated in Table 3 where $\lambda_{edge} = 0.681$ in Fig. 4(b) equals $\lambda_{edge} = 0.681$ in Fig. 4(d), they are different as 0.0567 MPa · m$^{1-\lambda_{edge}} \neq 0.0485$ MPa · m$^{1-\lambda_{edge}}$ due to the plane strain condition $\varepsilon_z = 0$ in Fig. 4(b).

Fig. 7(a) shows the singular stress distribution around the interface corner A. And Fig. 7(b) shows the singular stress distribution around the interface edge B. The solid lines indicate the asymptotic solutions obtained by substituting the singularity indexes in Table 2 and the ISSFs in Table 4 into Eq. (11). In Fig. 7(a) and (b), since the asymptotic solutions overlap the FEM stress distributions, it can be confirmed that the λ_{cor} and the λ_{edge} in Table 2 and the K_σ^{cor} and the K_σ^{edge} in Table 4 are calculated accurately.

In Section 2, the mesh-independent analysis methods were proposed for the singularity index and the ISSF for the 3D bonded structure. In this Section 3, the validity and accuracy of the proposed methods were confirmed. Although this paper assumes that the 3D corner has a real singularity index, there are other cases that the 3D corner has more than one real and complex singularities depending on the corner geometry and the material combination. The proposed mesh-independent analysis method can be extended to such cases. For example, the authors' previous study discussed the ISSF analysis method useful for two real singularity indexes in 2D bonded structures[45].

4. Adhesive strength of ABA butt joint (BJ-ABA) expressed as a constant ISSF at the interface corner and at interface edge

4.1. Singular stress distributions at the interface corner and the interface edge

The difference of the critical singular stress distributions will be discussed at the interface corner and at the interface edge in the 3D ABA joint by using the experimental results[46]. Fig. 8 shows the schematic illustration of the 3D ABA joint. Note the 3D butt joint with the similar adherends is named 3D BJ-ABA model, and 3D butt joint with the dissimilar adherends is named 3D BJ-ABC model. The model consists of two prismatic adherends (Materials 1 and 3) with length L, width W and depth D and thin adhesive layer (Material 2) of thickness h sandwiched between them. $L = W = D = 12.7$ mm is set. The h is changed from 0.05 mm to 5 mm. The remote uniform tensile stress $\sigma_y^\infty = \sigma_0 = 1$ MPa is set. Table 5 shows Young's moduli, Poisson's ratios of the adherend and adhesives, Dundurs' parameters, the singularity index λ_{2D} and the dimensionless ISSF $F_{\sigma,W}^{2D*}$ [$= K_\sigma^{2D*} / (\sigma_0 W^{1-\lambda_{2D}})$] for the 2D AB joint model. 0.35 % carbon steel (JIS S35C) was used as the adherend. Two kinds of epoxy resins were used as the adhesive. The epoxy resins A and B are a brittle adhesive and a ductile adhesive, respectively.

Fig. 9 shows the singular stress distributions at the interface corner A and the interface edge B under $\sigma_0 = 1$ MPa. The solid lines are the singular stress distributions at the interface corner A expressed with $\sigma_y^{cor} = K_\sigma^{cor} / r^{1-\lambda_{cor}}$. The dashed lines are the singular stress distributions at the interface edge B expressed with $\sigma_y^{edge} = K_\sigma^{edge} / r^{1-\lambda_{edge}}$. Then, the colored circle marks are the intersections of the σ_y^{cor} and the σ_y^{edge} with same adhesive thickness h. When $0.05\text{mm} \leq h \leq 2.0\text{mm}$, there are the circle marks within the range of $7\mu\text{m} \leq r \leq 270\,\mu\text{m}$. Since there is about only 10 % difference between the λ_{cor} and the λ_{edge}, the similar singular stress distributions are

(a)   Interface corner A.   (b)   Interface edge B.
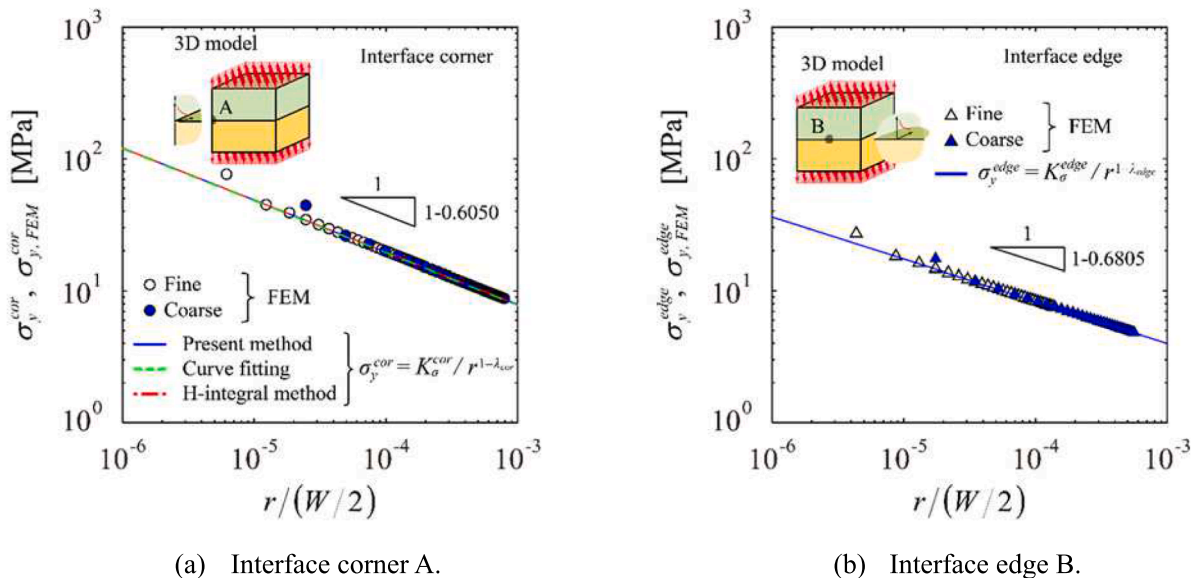
Fig. 7. Singular stress distribution at the interface corner A and singular stress distribution at the interface edge B in Fig. 4(d) (see AB joint in Fig. 4 (d), A = Si, B = Epoxy resin, $W = 2$ mm and $\sigma_y^\infty = \sigma_0 = 1$ MPa). In Fig. 7(a), (b), several plots may have some FEM errors, but they can be eliminated by taking the ratio with the reference solution by applying the same FEM mesh pattern.
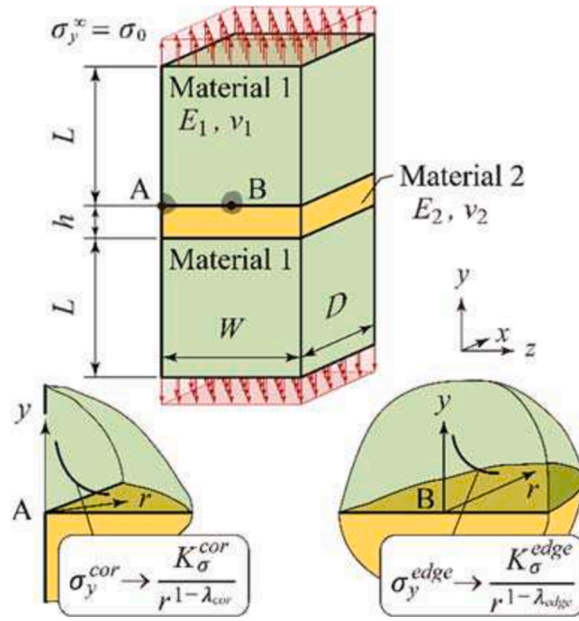
Fig. 8. Schematic illustration of 3D butt joint named BJ-ABA in this study (BJ = Butt Joint, A = Material 1, B = Material 2).

Table 5
Material properties used in the BJ-ABA in the present analyses[42,43].

Adherend Material	E_1 [GPa]	ν_1	Adhesive Material	E_2 [GPa]	ν_2	α	β	λ_{2D}	$F_{\sigma,W}^{2D*}$
Steel	210.0	0.3	Epoxy Resin A	3.14	0.37	0.969	0.199	0.684	0.405
(JIS 35C)	210.0	0.3	Epoxy Resin B	2.16	0.38	0.978	0.188	0.673	0.404

(a)   A = S35C, B = Epoxy resin A.

(b)   A = S35C, B = Epoxy resin B.
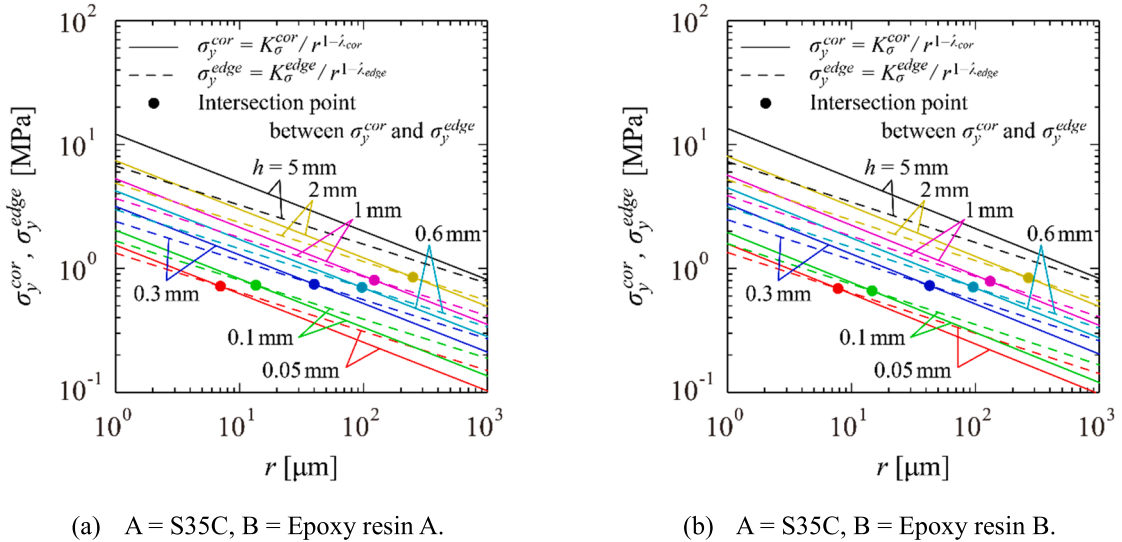
Fig. 9. Singular stress distribution $\sigma_y^{cor} = K_\sigma^{cor}/r^{1-\lambda_{cor}}$ at the interface corner and singular stress distribution $\sigma_y^{edge} = K_\sigma^{edge}/r^{1-\lambda_{edge}}$ at the interface edge in the 3D BJ-ABA model under $\sigma_0 = 1$ MPa (see BJ-ABA in Fig. 1(a), A = S35C, B = Epoxy resin A or Epoxy resin B).

formed at the interface corner and the interface edge.

Fig. 10 shows the critical singular stress distributions at the interface corner A and the interface edge B under $\sigma_0 = \sigma_c$, where the σ_c is the critical failure stress and is shown in Table 8. The solid lines denote the singular stress distributions at the interface corner A

(a) A = S35C, B = Epoxy resin A.

(b) A = S35C, B = Epoxy resin B.
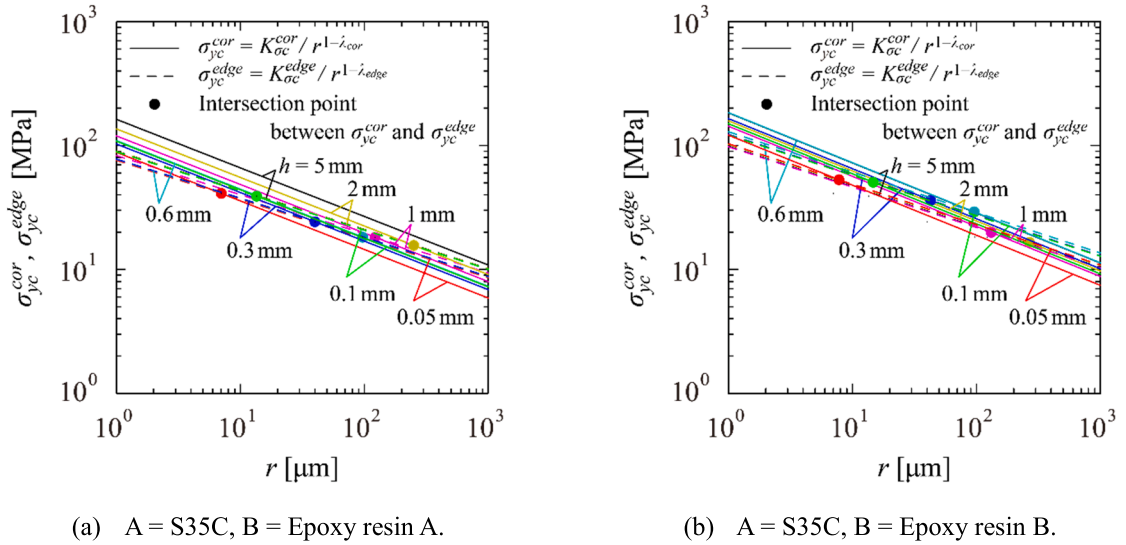
Fig. 10. Critical singular stress distribution $\sigma_{yc}^{cor} = K_{\sigma c}^{cor}/r^{1-\lambda_{cor}}$ at the interface corner and critical singular stress distribution $\sigma_{yc}^{edge} = K_{\sigma c}^{edge}/r^{1-\lambda_{edge}}$ at the interface edge under $\sigma_0 = \sigma_c$ (see BJ-ABA in Fig. 1(a), A = S35C, B = Epoxy resin A or Epoxy resin B).

expressed with $\sigma_{yc}^{cor} = K_{\sigma c}^{cor}/r^{1-\lambda_{cor}}$. The dashed lines denote the singular stress distributions at the interface edge B expressed with $\sigma_{yc}^{edge} = K_{\sigma c}^{edge}/r^{1-\lambda_{edge}}$. Then, the circle marks denote the intersections of the σ_{yc}^{cor} and σ_{yc}^{edge} with the same h and correspond to those in Fig. 9. The σ_{yc}^{cor} and the σ_{yc}^{edge} are similar within the range of $7\,\mu m \le r \le 270\,\mu m$ independent of the h.

Fig. 11 shows the average critical singular stress distributions at the interface corner A and the interface edge B which are given by the average of the critical ISSFs. When B = epoxy resin A, $K_{\sigma c,ave}^{cor} = 0.526\,MPa \cdot m^{1-\lambda_{cor}}$ and $K_{\sigma c,ave}^{edge} = 1.058\,MPa \cdot m^{1-\lambda_{edge}}$. The $\sigma_{yc,ave}^{cor}$ and $\sigma_{yc,ave}^{edge}$ intersect at $r = 101.3\,\mu m$. Then, when B = epoxy resin B, $K_{\sigma c,ave}^{cor} = 0.595\,MPa \cdot m^{1-\lambda_{cor}}$ and $K_{\sigma c,ave}^{edge} = 1.227\,MPa \cdot m^{1-\lambda_{edge}}$. The $\sigma_{yc,ave}^{cor}$ and $\sigma_{yc,ave}^{edge}$ intersect at $r = 93.1\,\mu m$. It can be confirmed that the roughly equal singular stress distributions are formed at the interface corner and along the interface edge independent of the h when $\sigma_0 = \sigma_c$.

As shown in Fig. 11, the critical singular stress distributions causing debonding are similar at the interface corner and at the interface edge. As shown in Fig. A2(d) in Appendix A, however, the largest ISSF region at the interface corner is much smaller than the large ISSF region along the interface edge (detail can be seen in Ref [63]). This is the reason why the debonding failure does not always

(a) A = S35C, B = Epoxy resin A.

(b) A = S35C, B = Epoxy resin B.
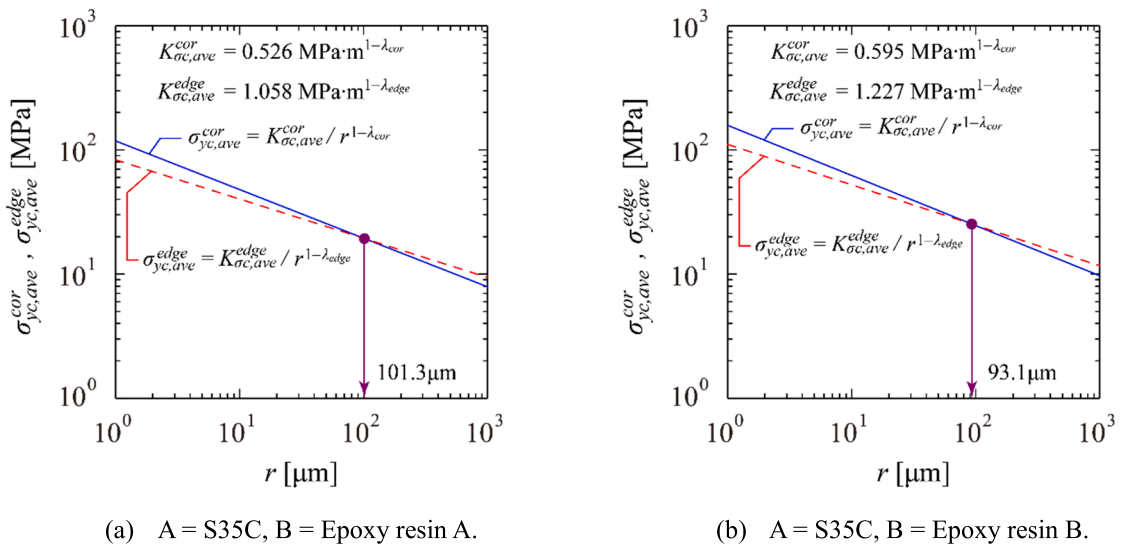
Fig. 11. Average critical singular stress distribution $\sigma_{yc,ave}^{cor} = K_{\sigma c,ave}^{cor}/r^{1-\lambda_{cor}}$ at the interface corner and critical average singular stress distribution $\sigma_{yc,ave}^{edge} = K_{\sigma c,ave}^{edge}/r^{1-\lambda_{edge}}$ at the interface edge under $\sigma_0 = \sigma_c$ (see BJ-ABA in Fig. 1(a), A = S35C, B = Epoxy resin A or Epoxy resin B).

occur at interface corner and the debonding often occurs at the interface edge even though the value of λ_{cor} is about 10 % smaller (more severe stress state) than the value λ_{edge}[63].

4.2. ISSF at the interface corner and ISSF at the interface edge

The ISSFs at the interface corner A and the interface edge B are computed by changing the h. Table 6 shows Young's moduli and Poisson's ratios of the materials used in numerical simulations. The epoxy resin is used in the adhesive. Steel (JIS SS400) and Al alloy (JIS A5052) are used in the adherends[64]. Table 7 shows Dundurs' parameter (α, β), the 3D corner and edge singularity indexes λ_{cor} and λ_{edge}, the dimensionless ISSF for the 2D AB joint in Fig. 2(b), $F_{\sigma,W}^{2D*}$ [$= K_{\sigma}^{2D*}/(\sigma_0 W^{1-\lambda_{2D}})$].

Fig. 12 and Table 8 show the dimensionless ISSFs $F_{\sigma,h}^{cor}$ and $F_{\sigma,h}^{edge}$ at the interface corner A and the interface edge B in the 3D BJ-ABA model, where $F_{\sigma,h}^{cor}$ and $F_{\sigma,h}^{edge}$ are defined as follows.

$$F_{\sigma,h} = \frac{K_{\sigma}}{\sigma_0 h^{1-\lambda}} \tag{25}$$

As shown in Table 8, when $h \leq 1.0$ mm, the $F_{\sigma,h}^{cor}$ and $F_{\sigma,h}^{edge}$ are constant independent of the h. Therefore, when $h \ll W$, $F_{\sigma,h}^{cor} \simeq 0.33$ and $F_{\sigma,h}^{edge} \simeq 0.38$ for the steel adherend, and $F_{\sigma,h}^{cor} \simeq 0.37$ and $F_{\sigma,h}^{edge} \simeq 0.41$ for the Al alloy adherend.

4.3. Critical ISSFs of BJ-ABA expressed as a constant ISSF

Table 9 and Fig. 13 show the critical ISSFs for the BJ-ABA with the steel adherend and the epoxy adhesive at the failure in Section 4.1, $K_{\sigma c}^{cor}$, $K_{\sigma c}^{edge}$ and $K_{\sigma c}^{2D}$. In the case of both epoxy adhesives (Resin A and Resin B), the failure stress σ_c decreases with increasing the h as shown in Table 9. As shown in Fig. 13(a) and (b), however, the $K_{\sigma c}^{cor}$ and $K_{\sigma c}^{edge}$ values are each plotted in the narrow bands with $\pm 10\%$ width around the average and approximately constant independent of the adhesive layer thickness h. Then, the $K_{\sigma c}^{edge}$ values almost correspond to the $K_{\sigma c}^{2D}$ values. That is because the roughly equal singular stress distributions are formed at the interface corner and along the interface edge independent of the h when $\sigma_0 = \sigma_c$ as mentioned in Sect. 4.1. In fact, it has been reported that the fracture origins were observed along the interface edge more frequently than at the interface corner[63]. Therefore, the debonding strength can be evaluated by using both conditions $K_{\sigma}^{cor} = K_{\sigma c}^{cor}$ and $K_{\sigma}^{edge} = K_{\sigma c}^{edge}$. Since the interface edge in the 2D BJ model is equivalent to the interface edge in the 3D BJ model, the 2D BJ model can be used to evaluate the debonding strength as well as the 3D BJ model. In Fig. 13, ISSF values at the 3D corner and the edge cannot be compared directly since they have different units depending on the singularity exponents. Fig. 13 shows that the adhesive strength can be expressed as a constant value of those ISSFs.

Fig. 13 is based on linear elastic analysis. One may think the effect of adhesive plasticity should be discussed since most adhesives are not linear elastic. Fig. 14 shows the stress–strain relation of the bulk adhesive and the stress–strain relations of the adhesive layers in a metal/resin butt joint. In Fig. 14, σ_y^{∞} is the remote tensile stress, ε_y^{Bulk} is the strain of the bulk adhesive, ε_y^{Resin} is the strain of the adhesive layers, and the adhesive layer thickness is changed as $h = 0.05, 0.1, 0.3, 0.6, 1.0, 2.0$ mm [65]. As shown in Fig. 14, although the bulk adhesive $\sigma_y^{\infty} - \varepsilon_y^{Bulk}$ relation shows the non-linear elastic behavior, the adhesive layer $\sigma_y^{\infty} - \varepsilon_y^{Resin}$ relation shows the linear elastic behavior independent of the adhesive layer thickness. That is because the adhesive layer is constrained by the adherends. Fig. 14 shows Young's modulus of the adhesive layer coincides with the constrained Young's modulus of the resin $E_y^{*Resin} = (1-\nu)/[(1-2\nu)(1+\nu)]E_y^{Resin} = 4.05$ GPa. The FEM elastic–plastic analysis showed that the plastic zone size $r_p^{FEM} \simeq 12$ μm satisfies the small-scale yielding condition $r_p^{FEM} \ll W$[65] independent of the adhesive layer thickness. Those findings provide the validity of the adhesive strength being expressed as a constant ISSF in Fig. 13 based on the linear elastic analysis.

5. Comparison of critical ISSFs focusing on AB interface between ABC joints and ABC joints

5.1. ISSF difference focusing on AB interface between BJ-ABA and BJ-ABC

In this Section 5, bonded dissimilar materials will be newly considered. Fig. 15 illustrates the 3D butt joint named BJ-ABC in this study (BJ = Butt Joint, A = Material 1, B = Material 2, C = Material 3). The ISSF of BJ-ABC will be analyzed and compared with the ISSF of 3D BJ-ABA. The adherends A, C and the adhesive B in Table 6 are used. Fig. 16 and Table 10 show the dimensionless ISSFs, $F_{\sigma,h}^{cor}$

Table 6
Young's moduli and Poisson's ratios of the materials used in numerical simulations [64].

Material	E[GPa]	ν
Steel (JIS SS400)	206	0.30
Al alloy (JIS A5052)	70	0.34
Epoxy resin	3.34	0.38

Table 7
Dundurs' parameter (α, β) and singularity indexes λ_{cor} and λ_{edge}.

Material combination	α	β	λ_{cor}	λ_{edge}	$F_{\sigma,W}^{2D*}$
Steel / epoxy resin	0.9661	0.1854	0.6043	0.6800	0.411
Al alloy / epoxy resin	0.9060	0.1731	0.6462	0.7122	0.445
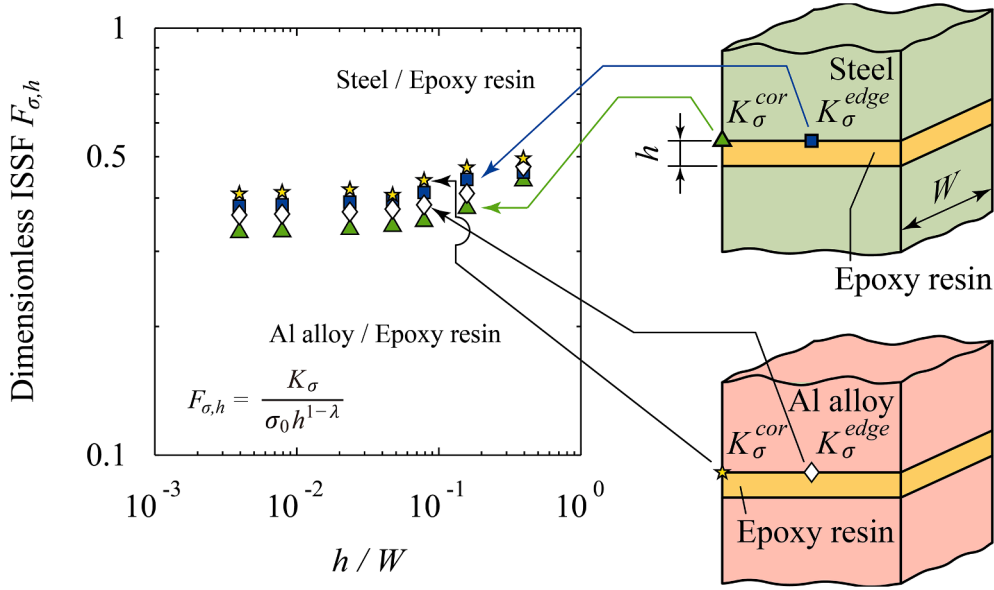
Fig. 12. Dimensionless ISSFs $F_{\sigma,h}^{cor} = K_{\sigma}^{cor}/(\sigma_0 h^{1-\lambda_{cor}})$ and $F_{\sigma,h}^{edge} = K_{\sigma}^{edge}/(\sigma_0 h^{1-\lambda_{edge}})$ for the 3D BJ-ABA (A = Steel, B = Epoxy resin).

Table 8
Dimensionless ISSFs $F_{\sigma,h}^{cor} = K_{\sigma}^{cor}/(\sigma_0 h^{1-\lambda_{cor}})$ and $F_{\sigma,h}^{edge} = K_{\sigma}^{edge}/(\sigma_0 h^{1-\lambda_{edge}})$ by varying the adhesive thickness h for the 3D BJ-ABA (A = Steel, B = Epoxy resin).

h[mm]	Steel adherend		Al alloy adherend	
	Interface corner A	Interface edge B	Interface corner A	Interface edge B
0.05	0.332	0.383	0.365	0.410
0.1	0.334	0.386	0.367	0.413
0.3	0.338	0.391	0.371	0.419
0.6	0.344	0.400	0.377	0.427
1.0	0.353	0.412	0.386	0.440
2.0	0.379	0.442	0.410	0.472
5.0	0.439	0.460	0.474	0.496

$[= K_{\sigma}^{cor}/(\sigma_0 h^{1-\lambda_{cor}})]$ at the interface corner A and $F_{\sigma,h}^{edge}$ $[= K_{\sigma}^{edge}/(\sigma_0 h^{1-\lambda_{edge}})]$ at the interface edge B in BJ-ABC. When the adhesive thickness h is small enough, $F_{\sigma,h}^{cor}$ and $F_{\sigma,h}^{edge}$ are not constant and they vary depending on h. This is because the upper and lower interfaces interfere with each other.

Fig. 17 shows the ratio of the ISSF for the 3D BJ-ABC model to the ISSF for the 3D BJ-ABA model. The ISSF ratios at the Al/epoxy interface corner and edge decrease with decreasing h. On the other hand, the ISSF ratios at the steel/epoxy interface corner and edge increase as the h decreases. Moreover, the ISSF ratio at the steel/epoxy interface corner is larger than that at the steel/epoxy interface edge. Note that the ISSF ratios can be compared because of dimensionless. When $h = 0.05$ mm, the ISSF ratio at the steel/epoxy interface corner is about 1.73, and the ISSF ratio at the steel/epoxy interface edge is about 1.43. When the opposite adherend is changed from the steel to the Al alloy, the ISSF at the steel/epoxy interface corner changes about 20 % larger than that at the steel/ epoxy interface edge. Therefore, when the one side of the adherends is changed, the ISSF at the interface corner with the smallest singularity index is strongly influenced.

Table 9

Critical ISSFs obtained thrrough 2D modeling $K_{\sigma c}^{2D}$ and through 3D modeling $K_{\sigma c}^{cor}$, $K_{\sigma c}^{edge}$ for BJ-ABA in Fig. 8 [A = S35C, B = Epoxy resin A in Table 5(a) or Epoxy resin B in Table 5(b)]. Note that in BJ-ABA, plane strain condition appears more significantly compared to AB joint corresponding to extremely large h when $h/W \geq 1$.

(a) A = S35C, B = Epoxy resin A in Fig. 8

h[mm]	σ_c[MPa] [37]	2D model	3D model	
		$K_{\sigma c}^{2D}$[MPa $\cdot$ m$^{1-\lambda_{2D}}$]	$K_{\sigma c}^{cor}$[MPa $\cdot$ m$^{1-\lambda_{cor}}$]	$K_{\sigma c}^{edge}$[MPa $\cdot$ m$^{1-\lambda_{edge}}$
0.05	57.2	0.970	0.392	0.966
0.1	53.3	1.120	0.482	1.130
0.3	32.5	0.978	0.458	0.989
0.6	25.9	0.981	0.487	0.983
1.0	22.6	1.017	0.532	1.055
2.0	18.4	1.071	0.606	1.138
5.0	13.4	1.135	0.724	1.144
Average		1.039	0.526	1.058

$\lambda_{2D} = \lambda_{edge} = 0.684$, $\lambda_{cor} = 0.608$

(b) A = S35C, B = Epoxy resin B in Fig. 8

h[mm]	σ_c[MPa] [37]	2D model	3D model	
		$K_{\sigma c}^{2D}$[MPa $\cdot$ m$^{1-\lambda_{2D}}$]	$K_{\sigma c}^{cor}$[MPa $\cdot$ m$^{1-\lambda_{cor}}$]	$K_{\sigma c}^{edge}$[MPa $\cdot$ m$^{1-\lambda_{edge}}$
0.05	76.8	1.147	0.457	1.144
0.1	71.4	1.339	0.565	1.346
0.3	49.7	1.342	0.621	1.361
0.6	41.2	1.411	0.694	1.428
1.0	25.3	1.042	0.539	1.082
2.0	19.7	1.060	0.596	1.132
5.0	13.6	1.085	0.691	1.094
Average		1.204	0.595	1.227

$\lambda_{2D} = \lambda_{edge} = 0.674$, $\lambda_{cor} = 0.596$

5.2. Comparison of critical ISSF between BJ-ABA and BJ-ABC (BJ = butt Joint)

In this Section, the debonding strength for the butt joints with similar/dissimilar adherends by the 3D model will be discussed by using the experimental results[66,67]. The tensile tests were performed on the BJ specimens with similar/dissimilar adherends in Fig. 8 and Fig. 14 when $L = W = 32$ mm, $D = 9$ mm and $h = 0.1$ mm. Steel (JIS SS400) and Cu alloy (JIS C2800) were used as the adherend. The epoxy resin was used in the adhesive. Table 11 shows Young's moduli and Poisson's ratios of the steel and epoxy resin. Table 12 shows Dundurs' parameter (α, β), the 3D corner and edge singularity indexes λ_{cor} and λ_{edge}, the dimensionless ISSF for the 2D AB joint in Fig. 2(b), $F_{\sigma,W}^{2D*}$ [$= K_{\sigma}^{2D*}/(\sigma_0 W^{1-\lambda_{2D}})$]. The combination of the steel and the epoxy has smaller singularity indexes than the combination of the Cu ally and epoxy. The steel and the epoxy resin are chosen as the materials 1 and 2, respectively. Then, the steel and the Cu alloy are chosen as the materials 3 for the similar adherends and the dissimilar adherends, respectively.

The dimensionless ISSFs at the steel/epoxy resin interfaces in the 3D BJ-ABA and the 3D BJ-ABC, $F_{\sigma,h}^{cor} = K_{\sigma}^{cor}/(\sigma_0 h^{1-\lambda_{cor}})$ and $F_{\sigma,h}^{edge} = K_{\sigma}^{edge}/(\sigma_0 h^{1-\lambda_{edge}})$, are shown in Table 13, where the $F_{\sigma,h}^{cor}$ and the $F_{\sigma,h}^{edge}$ are the dimensionless ISSFs at the interface corner A and the interface edge B in Figs. 8 and 15, respectively. When one side of the adherends is changed from steel to Cu alloy, the $F_{\sigma,h}^{cor}$ increases by 0.119 (35.4 %) and the $F_{\sigma,h}^{edge}$ increases by 0.093 (24.1 %). The $F_{\sigma,h}^{cor}$ increases more significantly than the $F_{\sigma,h}^{edge}$.

Table 14 shows the critical tensile stress experimentally obtained σ_c, the critical ISSF at the steel/epoxy interface corner A, $K_{\sigma c}^{cor}$, and the critical ISSF at the steel/epoxy interface edge B, $K_{\sigma c}^{edge}$. When the one side of the adherend is changed from the steel to the Cu alloy, the critical tensile stress σ_c decreases by 7.5 MPa, that is, by 27.7 %. The critical 3D corner ISSFs $K_{\sigma c}^{cor}$ coincide each other within 0.07 MPa $\cdot$ m$^{1-\lambda_{cor}}$, that is, within 2 %. The critical 3D edge ISSF $K_{\sigma c}^{edge}$ values agree within 0.51 MPa $\cdot$ m$^{1-\lambda_{edge}}$, that is within 10.2 %. It is seen that the $K_{\sigma c}^{cor}$ values are almost constant independent of the adherend combination.

5.3. Comparison of critical ISSF between TSLJ-ABA and TSLJ-ABC (TSLJ = Three-Step lap Joint)

The adhesive strength for the three-step lap joint with similar/dissimilar adherends (named TSLJ-ABC in this paper) will be discussed by analyzing the ISSF and using the previous experimental results[64]. The four-point bending tests were performed on the TSLJ-ABC with similar/dissimilar adherends. Fig. 18 shows the schematic illustration of the 3D TSLJ-ABC with experimental dimensions $L = W = 32$ mm, $D = 9$ mm, $l = 9.2$ mm and $h = t = 0.1$ mm. Steel (JIS SS400) and Al alloy (JIS A5052) were used as the adherend. The epoxy resin was used in the adhesive. Young's moduli and Poisson's ratios of the adherends and the adhesive used in the experiment are shown in Table 6. Then, Dundurs' parameter (α, β), the 3D corner and edge singularity indexes λ_{cor} and λ_{edge}, the dimensionless ISSF for the 2D AB joint in Fig. 2(b), $F_{\sigma,W}^{2D*}$ [$= K_{\sigma}^{2D*}/(\sigma_0 W^{1-\lambda_{2D}})$] are shown in Table 7. The TSLJ-ABC is composed of A =
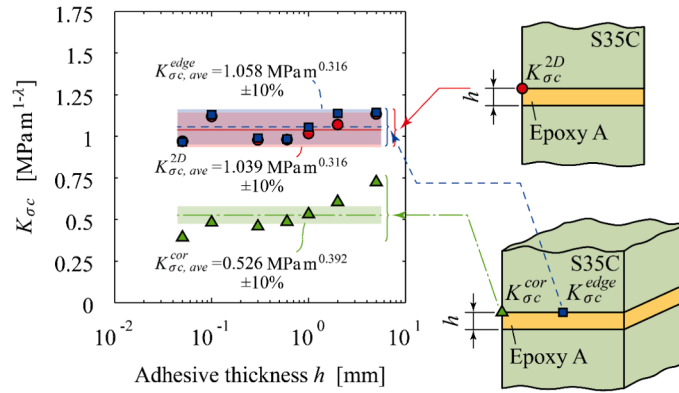
(a) A = S35C, B = Epoxy resin A in Fig. 8.
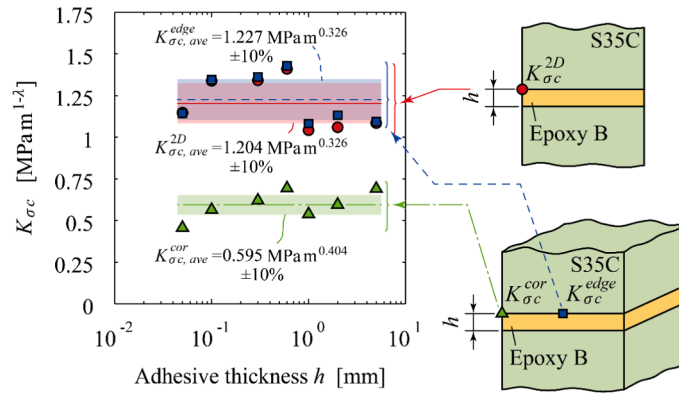
(b) A = S35C, B = Epoxy resin B in Fig. 8.

Fig. 13. Adhesive strength expressed as critical ISSF $K_{\sigma c}$ = const. in Fig. 8 independent of adhesive layer thickness h for BJ-ABA, A = S35C, B = Epoxy resin A in Fig. 13(a) and Epoxy resin B in Fig. 13(b). Note that in BJ-ABA, plane strain condition appears more significantly compared to AB joint corresponding to extremely large h when $h/W \geq 1$.
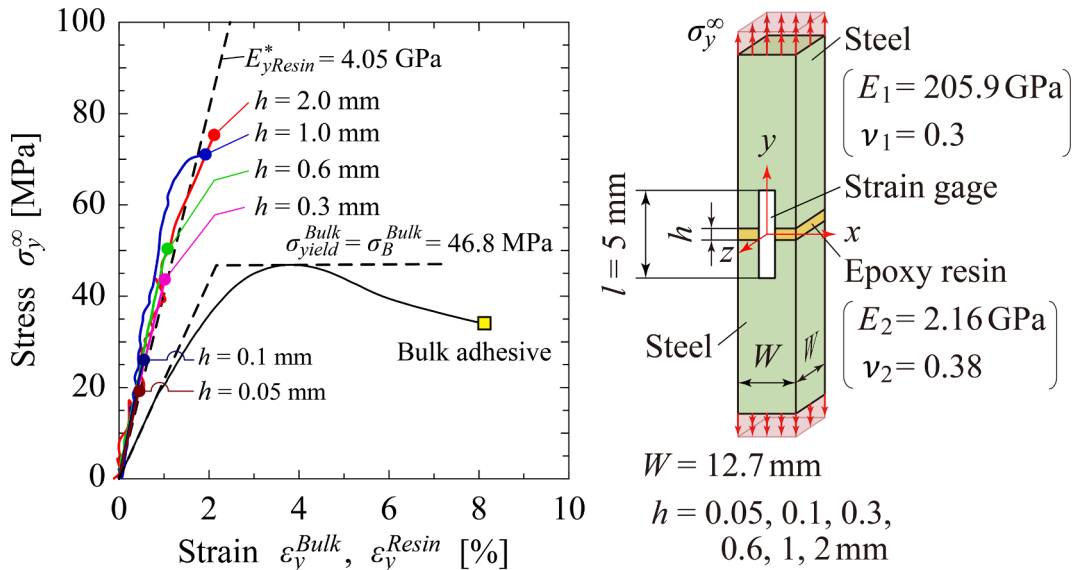
Fig. 14. $\sigma_y^\infty - \varepsilon_y^{Resin}$ relation of adhesive layer in butt joint for Resin B/S35C in comparison with $\sigma_y^\infty - \varepsilon_y^{Bulk}$ relation of bulk adhesive, where σ_y^∞ is a remote tensile stress, ε_y^{Bulk} a strain of an adhesive bulk, ε_y^{Resin} a strain of an adhesive layer[65].
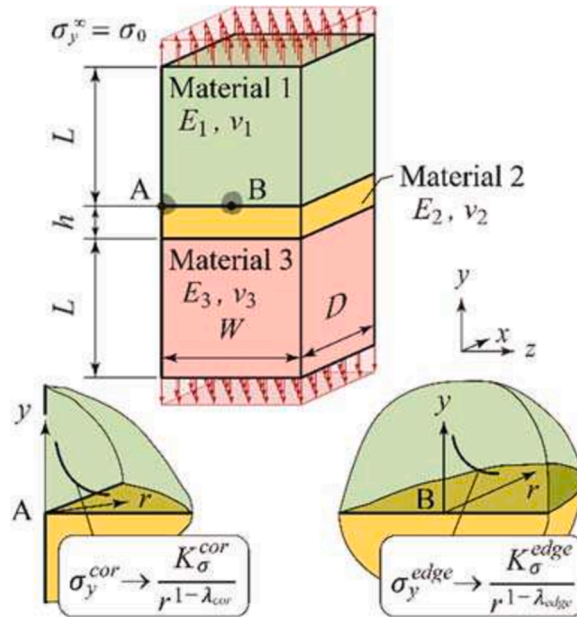
Fig. 15. Schematic illustration of the 3D butt joint named BJ-ABC in this study (BJ = Butt Joint, A = Material 1, B = Material 2, C = Material 3).
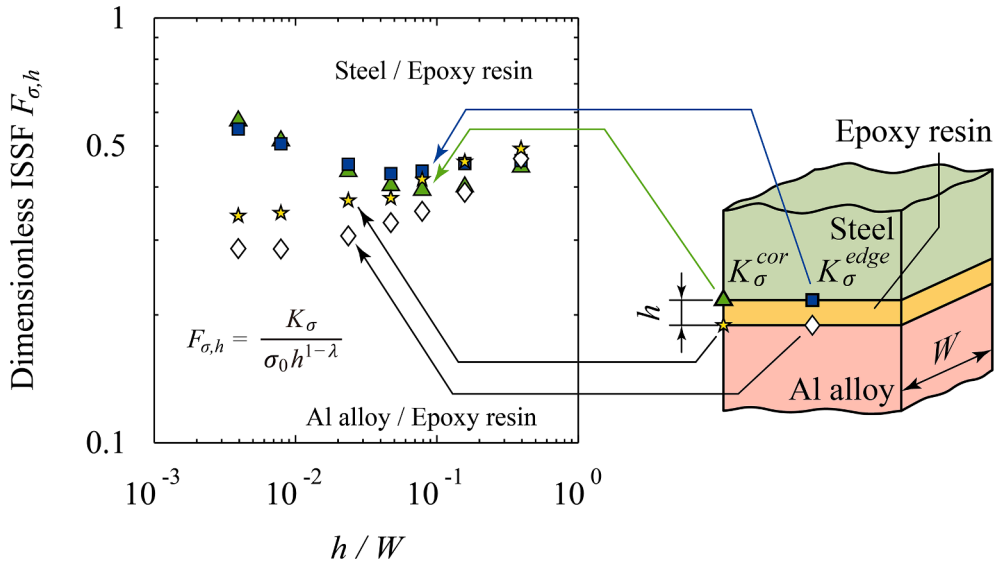
Fig. 16. Dimensionless ISSFs $F_{\sigma,h}^{cor}$ $[= K_{\sigma}^{cor}/(\sigma_0 h^{1-\lambda_{cor}})]$ and $F_{\sigma,h}^{edge}$ $[= K_{\sigma}^{edge}/(\sigma_0 h^{1-\lambda_{edge}})]$ for BJ-ABC (A = Steel, B = Epoxy resin, C = Al alloy). Both interfaces AB and BC are considered.

Steel, B = Epoxy resin, C = Al alloy. As shown in Table 7, the singularity index at the AB corner interface (= steel/epoxy corner interface), $\lambda_{cor} = 0.6043$, is the smallest among four singularity indexes. Since all debonding occurred at the AB interface in the experiments, the ISSF at the AB interface is considered.

The dimensionless ISSFs for the TSLJs with similar/dissimilar adherends, $F_{\sigma,h}^{cor}$ and $F_{\sigma,h}^{edge}$, are shown in Table 15, where the $F_{\sigma,h}^{cor}$ and the $F_{\sigma,h}^{edge}$ are the dimensionless ISSFs at the interface corner A and the interface edge B in Fig. 18, respectively. When one side of the adherends is changed from the steel to Al alloy, the $F_{\sigma,h}^{cor}$ increases by 0.0895 (27.8 %) and the $F_{\sigma,h}^{edge}$ increases by 0.0474 (12.7 %). The $F_{\sigma,h}^{cor}$ increases more significantly than the $F_{\sigma,h}^{edge}$, which suggests that the debonding is initiated from the interface corner easily than the

Table 10

Dimensionless ISSFs $F_{\sigma,h}^{cor}$ [$= K_{\sigma}^{cor}/(\sigma_0 h^{1-\lambda_{cor}})$] and $F_{\sigma,h}^{edge}$ [$= K_{\sigma}^{edge}/(\sigma_0 h^{1-\lambda_{edge}})$] for BJ-ABC (A = Steel, B = Epoxy, C = Al alloy). Both interfaces AB and BC are considered.

h[mm]	Steel/epoxy interface		Al/epoxy interface	
	Interface corner Point A	Interface edge Point B	Interface corner Point A	Interface edge Point B
0.05	0.573	0.548	0.287	0.343
0.1	0.514	0.505	0.286	0.347
0.3	0.435	0.453	0.307	0.372
0.6	0.403	0.436	0.330	0.394
1.0	0.393	0.436	0.351	0.417
2.0	0.401	0.455	0.389	0.459
5.0	0.446	0.463	0.467	0.493
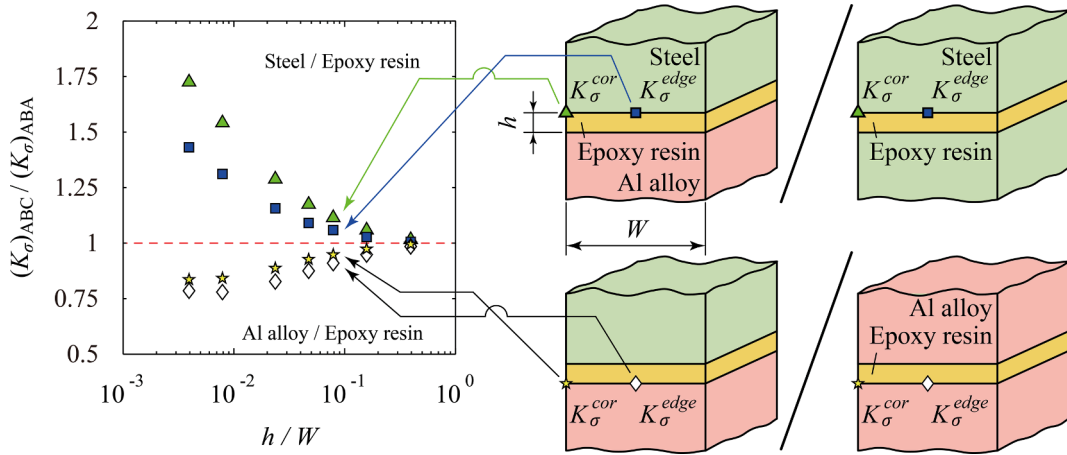
Fig. 17. ISSF for the 3D BJ-ABC in comparison with that for the 3D BJ-ABA (BJ = Butt joint, A = Steel, B = Epoxy, C = Al alloy). Both ISSFs at AB and CB interfaces are considered.

Table 11

Young's moduli and Poisson's ratios of the steel, Cu alloy and epoxy resin[66,67].

Material	E[GPa]	ν
Steel (JIS SS400)	209	0.29
Cu alloy (JIS C2800)	103	0.35
Epoxy resin	3.34	0.38

interface edge.

Table 16 shows the critical bending moment M_c experimentally obtained, the critical bending stress $\sigma_c = 6M_c/(DW^2)$, the critical ISSF at the steel/epoxy interface corner A, $K_{\sigma c}^{cor}$, and the critical ISSF at the steel/epoxy interface edge B, $K_{\sigma c}^{edge}$. When the one side of the adherend is changed from the steel to the Al alloy, the critical bending moment M_c decreases by 21.1N· m, that is, by 25.4 %. However, the critical 3D corner ISSF $K_{\sigma c}^{cor}$ coincides with each other within 0.021 MPa · m$^{1-\lambda_{cor}}$, that is, within 4.7 %. The critical 3D edge ISSF $K_{\sigma c}^{edge}$ coincides each other within 0.165 MPa · m$^{1-\lambda_{edge}}$, that is, within 15.7 %. It is seen that the $K_{\sigma c}^{cor}$ values are almost constant independent of the adherend combination. Fig. 19 shows (a) the critical ISSF at the steel/epoxy interface corner A, $K_{\sigma c}^{cor}$, and (b) the critical ISSF at the steel/epoxy interface edge B, $K_{\sigma c}^{edge}$ when the adhesive thickness $h = 0.1$ mm and $h \geq W = 32$ mm. The critical 3D corner ISSFs for TSLJ with $h = 0.1$ mm coincides that with $h \geq W = 32$ mm. It is seen that the adhesive strength of ABC joint can be expressed in a more suitable way by using the critical 3D interface corner as $K_{\sigma c}^{cor} = $ constant.

Table 12

Dundurs' parameter (α, β) and singularity indexes λ_{cor} and λ_{edge} for the material combinations of steel / epoxy resin and Cu alloy / epoxy resin.

Material combination	α	β	λ_{cor}	λ_{edge}	$F_{\sigma,W}^{2D*}$
Steel / epoxy resin	0.9664	0.1853	0.6040	0.6798	0.411
Cu alloy / epoxy resin	0.9356	0.1799	0.6266	0.6969	0.429

Table 13

Dimensionless ISSFs $F_{\sigma,h}^{cor}$ and $F_{\sigma,h}^{edge}$ both focusing on AB interface (= steel/epoxy interface). Comparison between BJ-ABA and BJ-ABC (BJ = Butt Joint, A = Steel, B = Epoxy resin, C = Cu alloy, $h = 0.1$mm).

Adherend combination	$F_{\sigma,h}^{cor} = K_{\sigma}^{cor}/(\sigma_0 h^{1-\lambda_{cor}})$ focusing on AB interface	$F_{\sigma,h}^{edge} = K_{\sigma}^{edge}/(\sigma_0 h^{1-\lambda_{edge}})$ focusing on AB interface
ABA	0.335	0.383
ABC	0.453	0.476

Table 14

Critical tensile stress σ_c experimentally obtained, critical 3D corner ISSF $K_{\sigma c}^{cor}$ and critical 3D edge ISSF $K_{\sigma c}^{edge}$ both focusing on AB interface (= steel/epoxy interface). Comparison between BJ-ABA and BJ-ABC (BJ = Butt Joint, A = Steel, B = Epoxy resin, C = Cu alloy, $h = 0.1$mm).

Adherend combination	σ_c[MPa] experimentally obtained [56,57]	$K_{\sigma c}^{cor}$[MPa · mm$^{1-\lambda_{cor}}$] focusing on AB interface	$K_{\sigma c}^{edge}$[MPa · mm$^{1-\lambda_{edge}}$] focusing on AB interface
ABA	27.1	3.65	4.97
ABC	19.6	3.57	4.46
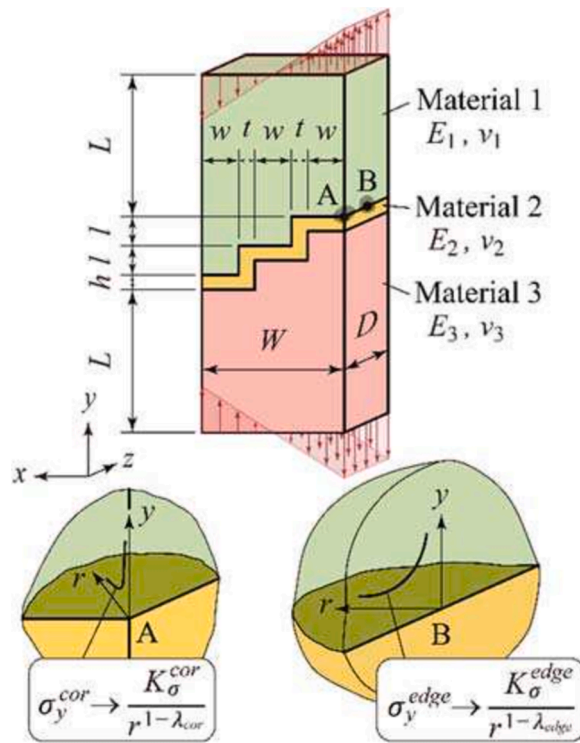
Fig. 18. Schematic illustration of three step lap joint named TSLJ-ABC in this study (TSLJ = Three-Step Lap Joint, A = Material 1, B = Material 2, C = Material 3). The experimental dimensions are $L = W = 32$ mm, $D = 9$ mm, $l = 9.2$ mm and $h = t = 0.1$ mm[64].

Table 15

Dimensionless ISSFs $F_{\sigma,h}^{cor}$ and $F_{\sigma,h}^{edge}$ focusing on the steel/epoxy interface. Comparison between TSLJ-ABA and TSLJ-ABC (TSLJ = Three-Step Lap Joint, A = Steel, B = Epoxy resin, C = Al alloy, $h = t = 0.1$ mm).

Adherend combination	$F_{\sigma,h}^{cor}[= K_{\sigma}^{cor}/(\sigma_0 h^{1-\lambda_{cor}})]$ focusing on AB interface	$F_{\sigma,h}^{edge}[= K_{\sigma}^{edge}/(\sigma_0 h^{1-\lambda_{edge}})]$ focusing on AB interface
ABA	0.322	0.372
ABC	0.411	0.419

Table 16

Critical bending moment M_c and critical bending stress σ_c both of which are obtained experimentally[64] and critical 3D corner ISSF $K_{\sigma c}^{cor}$ and critical 3D edge ISSF $K_{\sigma c}^{edge}$ both of which focus on AB interface (= steel/epoxy interface). TSLJ-ABA and TSLJ-ABC are compared (TSLJ = Three-Step Lap Joint, A = Steel, B = Epoxy resin, C = Cu alloy, $h = t = 0.1$ mm).

Adherend combination	M_c[N · m] experimentally obtained [64]	$\sigma_c = 6M_c/(DW^2)$ [MPa] experimentally obtained	$K_{\sigma c}^{cor}$[MPa · m$^{1-\lambda_{cor}}$] focusing on AB interface	$K_{\sigma c}^{edge}$[MPa · m$^{1-\lambda_{edge}}$] focusing on AB interface
ABA	83.0	54.0	0.452	1.054
ABC	61.9	40.3	0.431	0.889

(a) Critical 3D corner ISSF $K_{\sigma c}^{cor}$ (b) Critical 3D edge ISSF $K_{\sigma c}^{edge}$ (c) Three-Step Lap Joint, A = Steel, B = Epoxy resin, C = Cu alloy
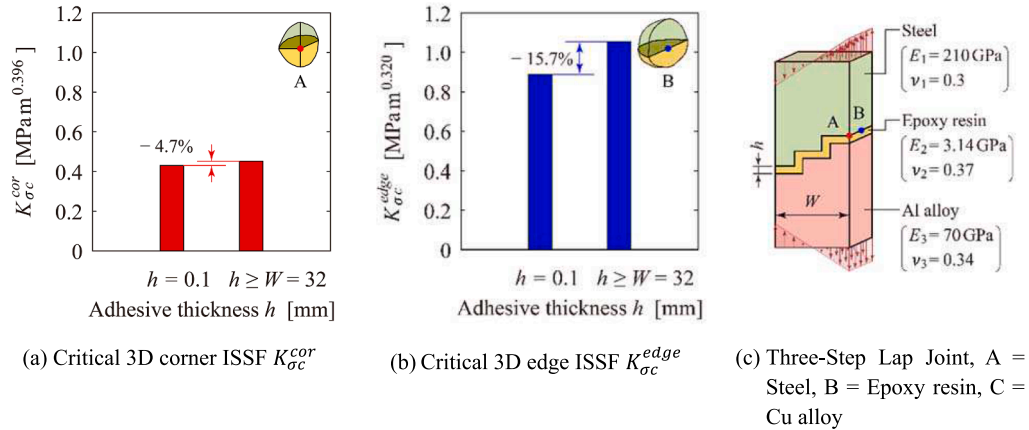
Fig. 19. Critical 3D corner ISSF $K_{\sigma c}^{cor}$ when $h = 0.1$ and $h \geq W = 32$ mm and critical 3D edge ISSF $K_{\sigma c}^{edge}$ are compared when $h = 0.1$ and $h \geq W = 32$ mm. Both ISSFs are on the AB interface (=steel/epoxy interface). The adhesive strength for TSLJ-ABC can be expressed as a constant ISSF in Fig. 19 (a) better than in Fig. 19(b). The results of TSLJ-ABC when $h \geq W = 32$ mm is corresponding to the results of AB joint (TSLJ = Three-Step Lap Joint, A = Steel, B = Epoxy resin, C = Cu alloy).

6. Conclusions

In this paper, an efficient method was proposed and named as the mesh-independent proportional method, which is useful for the ISSF at the interface corner as well as the singularity index λ in 3D dissimilar bonded joint. The validity and accuracy of the proposed methods were confirmed by analyzing the AB joints composed of A = Si and B = Epoxy. The adhesive strength was confirmed to be expressed as constant ISSF based on the previous experimental data for the ABA and ABC butt joints and the ABA and ABC three-step lap joints with similar/dissimilar adherends composed of A = Steel, B = Epoxy, C = Cu alloy. The conclusion can be summarized in the following way.

(1) By investigating relation between the minimum mesh size $e_{\min}$ and the FEM stresses $\sigma_{FEM}(r)$, mesh-independent formulas such as $\sigma_{FEM}(r) \cdot (e_{\min})^{1-\lambda} = $ const. [see Eq. (8)] were theoretically derived from the proportional stress fields in AB joints having similar FEM mesh pattern (see Fig. 3). This mesh-independent expression is extremely useful because it uses only two stress values instead of many stress values etc. in conventional analysis [see Eq. (24)]. The ISSF obtained by the proposed proportional method coincides with the previous results to the three digits (see Table 4).

(2) A mesh-independent formula [Eq. (9)] useful for 3D corner singularity index was also derived theoretically by considering AB joints having similar FEM mesh (see Fig. 3). The 3D corner singularity index was previously analyzed also by using complicated methods such as eigen analysis method. The singularity index obtained by the proposed proportional method coincides with the previous results to the three digits. It was confirmed that the singularity indexes and the ISSFs are determined accurately by using the mesh-independent proportional method.

(3) The critical singular stress distributions at debonding were compared at the interface corner and at the interface edge by using previous experimental data of BJ-ABA (see Figs. 10, 11). The roughly equal critical singular stress distributions were confirmed at the interface corner and at the interface edge independent of the adhesive thickness $h = 0.05$mm ~ 5mm. The results showed that the adhesive strength can be expressed as a constant ISSF by focusing on 2D edge ISSF, 3D edge ISSF, or 3D corner ISSF (see Fig. 13).

(4) Under unit remote tensile stress, the ISSF for the BJ-ABC is larger than the that for the BJ-ABA (see Fig. 17). The difference between the ABC and the ABA increases with decreasing the adhesive thickness especially at the interface corner compared to the interface edge. The adhesive strength was discussed based on the previous experimental data for the BJ-ABA/ABC and TSLJ-ABA/ABC. The adhesive strength of ABC joint can be expressed more suitably by focusing on the 3D interface corner (see Tables 14, 16, Fig. 19).

CRediT authorship contribution statement

Tatsujiro Miyazaki: Writing – review & editing, Writing – original draft, Formal analysis, Data curation, Conceptualization. **Hibiki Fukuda:** Data curation. **Nao-Aki Noda:** Writing – review & editing, Validation.

Declaration of competing interest

The authors declare that they have no known competing financial interests or personal relationships that could have appeared to influence the work reported in this paper.

Appendix A. Use of the term "ISSF" and its usefulness for evaluating adhesive strength

In fracture mechanics, the term "stress intensity factor (SIF)" has been successfully used to evaluate the intensity of singular stress fields (ISSF) for various cracks as shown in Figs. A1(a), (b). Fig. A1(c) shows that the SIF concept can be extended to sharp notch by changing the opening angle from zero to a certain value[68–71]. Also, Fig. A1(d) shows that it can be extended to inclusions having sharp corner whose singular stress field can be characterized Mode I and Mode II in a similar way of cracks[72,73]. In Figs. A1 (c), (d), the term "generalized stress intensity factor" are often used. Also, the SIF concept can be extended to interface cracks as shown in Fig. A1 (e) by using the term "stress intensity factor" or "interface stress intensity factor"[74]. In those problems in Figs. A1(c)-(e) and in Figs. A1(f), (g), the stress concentration due to geometry is corresponding to the stress concentration due to crack. For example, like the crack length "c" controlling the SIF in Figs. A1(a), (b), the notch and inclusion dimensions "c" control the GSIF in Figs. A1 (c)-(g).

However, in Figs. A1(h), (i), the stress concentration arises only from the material difference, not the geometry. In Figs. A1(h), (i), the ISSF is sometimes controlled by the plate width "W" and sometimes by the adhesive layer thickness "h". In other words, there are similarities between the cracks in Fig. A1(a), (b) and the notches in Fig. A1(c), (d) but not Figs. A1(h), (i). Therefore, this paper and authors' previous papers use the term "ISSF" consistently.
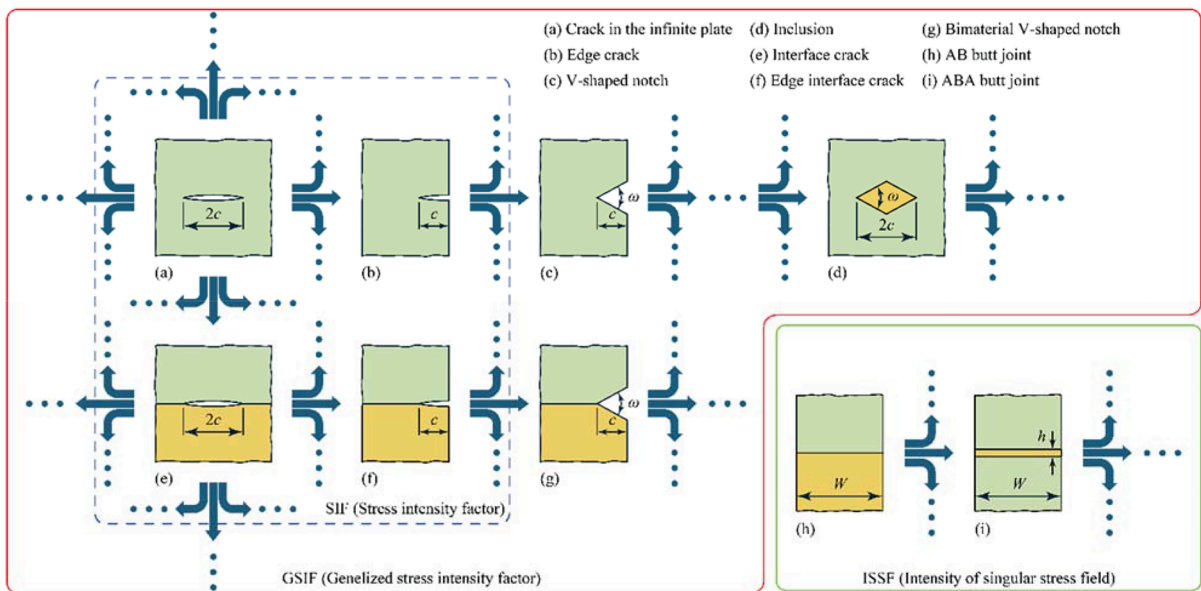
Fig. A1. Genealogical chart of various cracks and V-shaped notches and V-shaped inclusions in comparison with genealogical chart of AB- and ABA-joints.

The usefulness of the ISSF will be shown for the butt joint (BJ) specimen consisting of 0.35 % carbon steel adherend and epoxy adhesive[42,43]. Fig. A2 (a) shows the experimental results σ_c by varying the adhesive thickness $h = 0.05$ mm ~ 5 mm. The critical remote tensile stress $\sigma_0 = \sigma_c$ increases with decreasing the adhesive thickness h. Fig. A2 (b) shows the ISSFs analyzed at the interface edge in the 2D BJ model when the remote stress $\sigma_0 = 1$ MPa. The ISSF decreases with decreasing the adhesive thickness h. Fig. A2 (c) shows the critical ISSFs when the debonding failure occurs. The adhesive strength can be expressed as a constant critical ISSF independent of h as shown in Fig. A2 (c). The results in Fig. A2 (c) can be explained from Fig. A2 (a) and Fig. A2 (b). The critical ISSF obtained at the interface end in Fig. A2 (c) can be confirmed from the critical ISSF distributions at the interface edge in the 3D butt joint. Fig. A2 (d) shows that the critical ISSF $K_{\sigma c}$ distribution along the interface edge obtained from the 3D BJ model[19] almost coincides with the results in Fig. A2 (c). In this way, the 2D ISSF and the edge ISSF are useful for expressing the adhesive strength as a
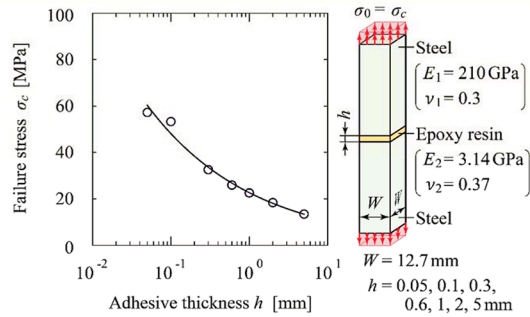
(a) Critical remote tensile stress σ_c obtained experimentally from Fig.1 (a) [42].
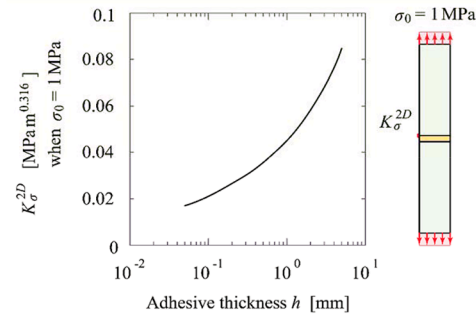
(b) ISSF K_σ^{2D} at the interface edge in the 2D BJ under a remote stress $\sigma_0 = 1$ MPa [43].
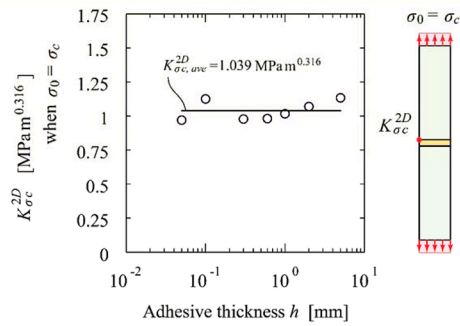
(c) Critical ISSF $K_{\sigma c}^{2D}$ obtained from the 2D BJ modeling [43].
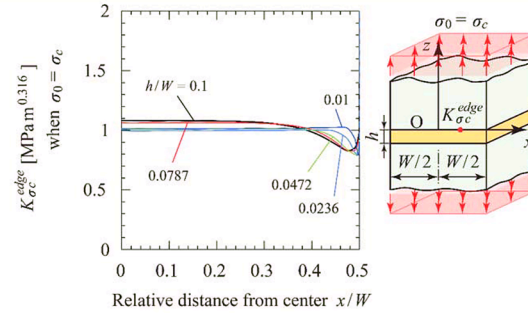
(d) Critical ISSF $K_{\sigma c}$ distribution along the interface edge obtained from the prismatic 3D BJ modeling [19].

Fig. A2. Critical ISSF distribution along the interface edge of the 3D prismatic BJ-ABA (BJ = butt joint, A = S35C, B = Epoxy resin). (a) Critical failure stress obtained experimentally [42], (b) ISSF for the 2D BJ under the remote stress MPa [47], (c) Critical ISSF obtained from the 2D BJ modelling [43], (d) Critical ISSF distribution along the interface edge obtained from the prismatic 3D BJ modelling [19].

constant value in most cases.

Appendix B. Bad pair conditions at the interface corner and interface edge in 3D butt joint

The material combination yielding the stress singularity at the interface corner and the interface edge is called the bad pair. The bad pair condition for the interface corner A in Fig. 2 (a) can be expressed by the discriminant Δ_{3D}^{cor} as follows[26].

$$\Delta_{3D}^{cor} = \left(\frac{\sqrt{1-\nu_1}}{E_1} - \frac{\sqrt{1-\nu_2}}{E_2} \right) \left(\frac{\nu_1}{E_1} - \frac{\nu_2}{E_2} \right) > 0 \tag{B1}$$

When the combination of material 1 and material 2 satisfies Eq. (B1), the singularity index at the interface corner A is real and smaller than 1 producing the singular stress field. On the other hand, the bad pair condition for the interface edge B can be expressed by the discriminant Δ_{3D}^{edge} as follows.

$$\Delta_{3D}^{edge} = \left(\frac{\nu_1 + \nu_1^2}{E_1} - \frac{\nu_2 + \nu_2^2}{E_2} \right) \left(\frac{1-\nu_1^2}{E_1} - \frac{1-\nu_2^2}{E_2} \right) > 0 \tag{B2}$$

When the combination of material 1 and material 2 satisfies Eq. (B2), the singularity index at the interface edge B is real and smaller than 1 producing the singular stress field. The condition (B2) can be rewritten in terms of Dundurs' parameter (α, β) as follows.

$$\Delta_{3D}^{edge*} = \Delta_{2D}^* = \alpha(\alpha - 2\beta) > 0 \tag{B3}$$

Fig. B1 (a) illustrates the bad pair condition (B1) and Fig. B1(b) illustrates the bad pair condition (B2) [26]. When the material combination satisfies Eq. (B1), the singular stress field in Eq. (10) $\sigma_y^{cor}(r) = K_\sigma^{cor}|_{\varphi=\pi/4}/r^{1-\lambda_{cor}}$ appears. Then, as shown in Fig. B1(a), the material combination belongs to regions I, II, III or IV. If the material combination belongs to region I or region II, the singular stress field does not appear at the interface edge as shown in Fig. B1.
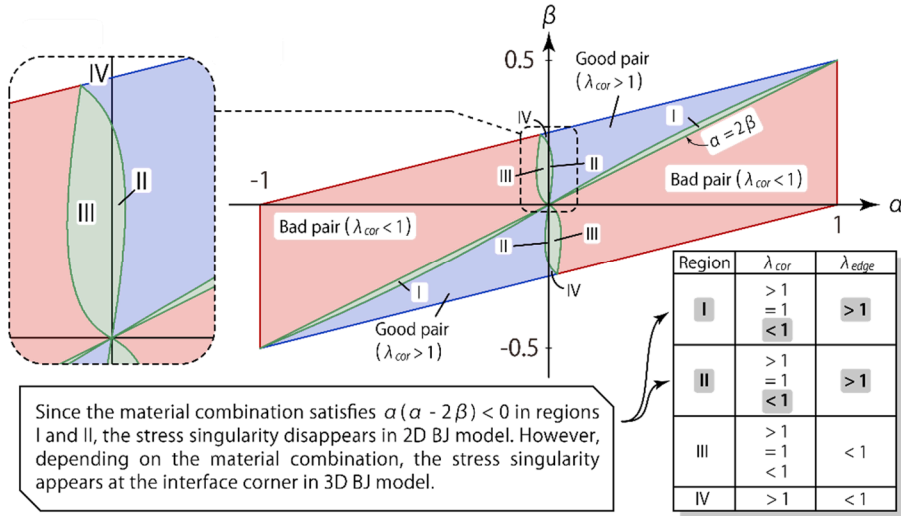
(a) 3D interface corner A
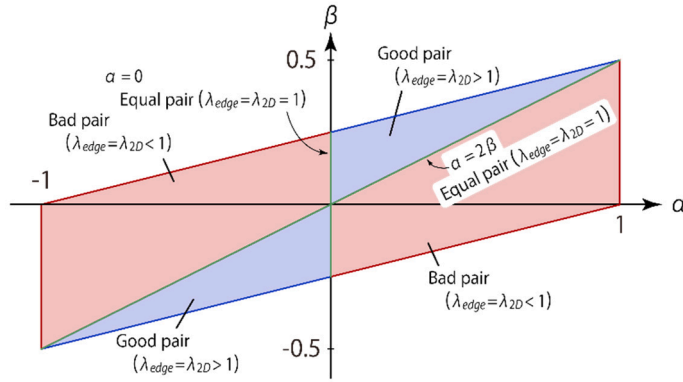
(b) 3D interface edge B

Fig. B1. Bad pair condition at 3D interface corner A and edge B in the BJ model on the α-β map [26].

Appendix C. Mesh-dependency of FEM stress $\sigma_{FEM}(r)$ and mesh-independency of the term "$\sigma_{FEM} \cdot (e_{\min})^{1-\lambda}$"

In Sect. 2.3, to clarify the variation of FEM stress depending on the minimum element size, the formula (8) was derived theoretically when FEM is applied to analyzing singular stress fields. When $(ne_0^{cor})^{1-\lambda_{cor}}$ is multiplied by both sides of Eq. (7), the following equation (8) is obtained.

$$\sigma_{y,FEM}^{cor(a)}(0)|_{e_{\min}=e_0^{cor}} \cdot \left(e_0^{cor}\right)^{1-\lambda_{cor}} = \sigma_{y,FEM}^{cor(b)}(0)|_{e_{\min}=ne_0^{cor}} \cdot \left(ne_0^{cor}\right)^{1-\lambda_{cor}} = \text{constant} \quad \text{(a-b relation 4)} \tag{8}$$

Equation (8) is important because it provides how the FEM stress $\sigma_{y,FEM}^{cor(a)}(0)|_{e_{\min}}$ varies depending on the minimum element size $e_{\min}$. Since the real stress at the interface corner diverges to infinity, the FEM provides only the approximate stress different from the real stress. Although the FEM stress depends on the mesh strongly, the relation between the FEM stress and the mesh is unknown. However, when the FEM analyses are performed by changing the $e_{\min}$ under the element shape kept constant at the interface corner, the FEM stress is inversely proportional to the $(e_{\min})^{1-\lambda_{cor}}$ as shown in Eq. (8).

Table C1 shows the FEM stresses in Fig. 4 (a), (b), (c) when $W = 2$ mm and $\sigma_y^\infty = 1$ MPa. As shown in Table C1(a), by varying the element size in the range $e_0^{edge}/(W/2) = 4.360 \times 10^{-6} \sim 1.744 \times 10^{-5}$, the FEM stress in Fig. 4(a) varies in the range $\sigma_{y,FEM}^{edge}(0) = 40.63 \sim 26.10$ depending on the element size e_0^{edge}. However, by multiplying by $\left(e_0^{edge}\right)^{1-\lambda_{edge}}$, the value of $\sigma_{y01,FEM}^{edge} \cdot \left(e_0^{edge}\right)^{1-\lambda_{edge}} =$

0.7907 becomes independent of the element size e_0^{edge}. This is because the mesh dependency of the FEM stress $\sigma_{y,FEM}^{edge}(0)$ around the singular point $r = 0$ can be eliminated by multiplying the FEM stress $\sigma_{y,FEM}^{edge}(0)$ by $(e_{min})^{1-\lambda}$. Table C1 confirms the mesh independency of Eq. (8) numerically.

Table C2 shows the FEM stresses in Fig. 4(d) at the interface corner A in and the interface edge B. By varying the element size in the range $e_0^{cor}/(W/2) = 4.360 \times 10^{-6} \sim 1.744 \times 10^{-5}$, the FEM stress varies in the range $\sigma_{y,FEM}^{cor}(0) = 104.9 \sim 60.64$ and $\sigma_{y,FEM}^{cor}(\sqrt{2}\,e_0^{cor}) = 76.58 \sim 44.29$. However, $\sigma_{y,FEM}^{cor}(0) \cdot (\sqrt{2}\,e_0^{cor})^{1-\lambda_{cor}} = 0.9172$ and $\sigma_{y,FEM}^{cor}(\sqrt{2}\,e_0^{cor}) \cdot (e_0^{cor})^{1-\lambda_{cor}} = 0.6699$ are independent of e_0^{cor}. This is because the mesh-dependency of the FEM stress near the singular point can be canceled by multiplying the FEM stress by $(e_{min})^{1-\lambda}$. Table C2 confirms the mesh independency of Eq. (8) numerically.

Table C1

Mesh-dependency of FEM stress $\sigma_{FEM}(r)$ and mesh-independency of $\sigma_{FEM}(r) \cdot (e_{min})^{1-\lambda}$ in Fig. 4(a) − (c). Table C1(a) considers Fig. 4(b) where FEM stress $\sigma_{FEM}(r) = \sigma_{y,FEM}^{edge}(0)$ and cubic element of edge length $e_{min} = e_0^{edge}$. Table C1(b) considers Fig. 4(c) where FEM stress $\sigma_{FEM}(r) = \sigma_{y,FEM}^{edge}(0)$ and square element of edge length $e_{min} = e_0^{edge}$. Table C1(c) considers Fig. 4(a) where FEM stress $\sigma_{FEM}(r) = \sigma_{y,FEM}^{edge}(0)$ and square element of edge length $e_{min} = e_0^{edge}$. Fig. 4(a), (c) when $W = 2$ mm and $\sigma_y^\infty = 1$ MPa.

(a) 3D AB joint in Fig. 4(b) where $\varepsilon_z = 0$ to obtain ISSF as an unknown problem.

$e_0^{edge}/(W/2)$	$\sigma_{y,FEM}^{edge}(0)$	$\sigma_{y,FEM}^{edge}(0) \cdot \left(e_0^{edge}\right)^{1-\lambda_{edge}}$	$\sigma_{y,FEM}^{edge}\left(e_0^{edge}\right)$	$\sigma_{y,FEM}^{edge}\left(e_0^{edge}\right) \cdot \left(e_0^{edge}\right)^{1-\lambda_{edge}}$
4.360×10^{-6}	40.63	0.7907	31.63	0.6157
1.744×10^{-5}	26.10	0.7907	20.32	0.6157

(b) 2D AB joint in Fig. 4(c) where $\varepsilon_z = 0$ to obtain ISSF as an unknown problem.

$e_0^{2D}/(W/2)$	$\sigma_{y,FEM}^{2D}(0)$	$\sigma_{y,FEM}^{2D}(0) \cdot \left(e_0^{2D}\right)^{1-\lambda_{2D}}$	$\sigma_{y,FEM}^{2D}\left(e_0^{2D}\right)$	$\sigma_{y,FEM}^{2D}\left(e_0^{2D}\right) \cdot \left(e_0^{2D}\right)^{1-\lambda_{2D}}$
3^{-12}	53.32	0.7898	41.51	0.6150
3^{-9}	18.60	0.7898	14.48	0.6149

(c) 2D AB joint in Fig. 4(a) to be used as a reference problem.

$e_0^{2D*}/(W/2)$	$\sigma_{y,FEM}^{2D*}(0)$	$\sigma_{y,FEM}^{2D*}(0) \cdot \left(e_0^{2D}\right)^{1-\lambda_{2D}}$	$\sigma_{y,FEM}^{2D*}\left(e_0^{2D}\right)$	$\sigma_{y,FEM}^{2D*}\left(e_0^{2D}\right) \cdot \left(e_0^{2D}\right)^{1-\lambda_{2D}}$
3^{-12}	52.79	0.7821	41.11	0.6090
3^{-9}	18.42	0.7820	14.34	0.6089

Table C2

Mesh-dependency of FEM stress $\sigma_{FEM}(r)$ and mesh-independency of $\sigma_{FEM}(r) \cdot (e_{min})^{1-\lambda}$ in Fig. 4(d). Table C2(a) referring to the corner in Fig. 4(d) where $\sigma_{FEM}(r) = \sigma_{y,FEM}^{cor}(0)$ and $e_{min} = \sqrt{2}e_0^{cor}$. Table C2(b) referring to the edge in Fig. 4(d) where $\sigma_{FEM}(r) = \sigma_{y,FEM}^{edge}(0)$ and $e_{min} = e_0^{edge}$. In Fig. 4(b), $W = 2$ mm and $\sigma_y^\infty = 1$ MPa.

(a) FEM stress at interface corner A.

$e_0^{cor}/(W/2)$	$\sigma_{y,FEM}^{cor}(0)$	$\sigma_{y,FEM}^{cor}(0) \cdot \left(\sqrt{2}\,e_0^{cor}\right)^{1-\lambda_{cor}}$	$\sigma_{y,FEM}^{cor}(\sqrt{2}e_0^{cor})$	$\sigma_{y,FEM}^{cor}(\sqrt{2}e_0^{cor}) \cdot \left(\sqrt{2}\,e_0^{cor}\right)^{1-\lambda_{cor}}$
4.360×10^{-6}	104.9	0.9172	76.58	0.6699
1.744×10^{-5}	60.64	0.9172	44.29	0.6699

(b) FEM stress at interface edge B.

$e_0^{edge}/(W/2)$	$\sigma_{y,FEM}^{cor}(0)$	$\sigma_{y,FEM}^{edge}(0) \cdot \left(e_0^{edge}\right)^{1-\lambda_{edge}}$	$\sigma_{y,FEM}^{edge}(e_0^{cor})$	$\sigma_{y,FEM}^{edge}(e_0^{cor}) \cdot \left(e_0^{edge}\right)^{1-\lambda_{edge}}$
4.360×10^{-6}	34.73	0.6764	27.04	0.5267
1.744×10^{-5}	22.32	0.6764	17.38	0.5267

Data availability

No data was used for the research described in the article.

References

[1] Goede M, Stehlin M, Rafflenbeul L, Kopp G, Beeh E. Super Light Car – lightweight construction thanks to a multi-material design and function integration. Eur Transp Res Rev 2009;1:5–10. https://doi.org/10.1007/s12544-008-0001-2.

[2] Kleemann S, Fröhlich T, Türck E, Vietor T. A methodological approach towards multi-material design of automotive components. Procedia CIRP 2017;60:68–73. https://doi.org/10.1016/j.procir.2017.01.010.

[3] Watson B, Nandwani Y, Worswick MJ, Cronin DS. Metallic multi-material adhesive joint testing and modeling for vehicle lightweighting. Int J Adhesion Adhes 2019;95:102421. https://doi.org/10.1016/j.ijadhadh.2019.102421.

[4] Naito J, Suzuki R. Multi-material Automotive Bodies and Dissimilar Joining Technology to Realize Multi-material. KOBELCO TECHNOLOGY REVIEW 2020;38: 32–7. https://www.kobelco.co.jp/english/ktr/pdf/ktr_38/032-037.pdf.

[5] Blanco D, Rubio EM, Marín MM, Davim JP. Advanced materials and multi-materials applied in aeronautical and automotive fields: a systematic review approach. Procedia CIRP 2021;99:196–201. https://doi.org/10.1016/j.procir.2021.03.027.

[6] Beber VC, Brede M. Multiaxial static and fatigue behaviour of elastic and structural adhesives for railway applications. Procedia Struct Integr 2020;28:1950–62. https://doi.org/10.1016/j.prostr.2020.11.018.

[7] Liu Y, Carnegie C, Ascroft H, Li W, Han X, Guo H, et al. Investigation of adhesive joining strategies for the application of a multi-material light rail vehicle. Mater 2021;14(22):6991. https://doi.org/10.3390/ma14226991.

[8] Delzendehrooy F, Akhavan-Safar A, Barbosa AQ, Beygi R, Cardoso D, Carbas RJC, et al. A comprehensive review on structural joining techniques in the marine industry. Compos Struct 2022;289(1):115490. https://doi.org/10.1016/j.compstruct.2022.115490.

[9] Barnes TA, Pashby IR. Joining techniques for aluminium spaceframes used in automobiles: Part II - adhesive bonding and mechanical fasteners. J Mater Process Technol 2000;99(1–3):72–9. https://doi.org/10.1016/S0924-0136(99)00361-1.

[10] Packham DE. Adhesive technology and sustainability. Int J Adhesion Adhes 2009;29:248–52. https://doi.org/10.1016/j.ijadhadh.2008.06.002.

[11] Tserpes K, Barroso-Caro A, Carraro PA, Beber VC, Floros I, Gamon W, et al. A review on failure theories and simulation models for adhesive joints. J Adhes 2021; 98(12):1855–915. https://doi.org/10.1080/00218464.2021.1941903.

[12] Ramalho LDC, Campilho RDSG, Belinha J, da Silva LFM. Static strength prediction of adhesive joints:A review. Int J Adhesion Adhes 2020;96:102451. https:// doi.org/10.1016/j.ijadhadh.2019.102451.

[13] Williams ML. Stress singularities resulting from various boundary conditions in angular corners of plates in extension. J Appl Mech 1952;19:526–8. https://doi. org/10.1115/1.4010553.

[14] Hein VL, Erdogan F. Stress singularities in a two-material wedge. Int J Fract Mech 1971;7:317–30. https://doi.org/10.1007/BF00184307.

[15] Dempsey JP, Sinclair GB. On the singular behavior at the vertex of a bi-material wedge. J Elasticity 1981;11:317–27. https://doi.org/10.1007/BF00041942.

[16] Reedy Jr ED, Guess TR. Interface corner failure analysis of joint strength: Effect of adherend stiffness. Int J Fract 1997;88:305–14. https://doi.org/10.1023/A: 1007436110715.

[17] Qian Z, Akisanya AR. An experimental investigation of failure initiation in bonded joints. Acta Mater 1998;46(14):4895–904. https://doi.org/10.1016/S1359-6454(98)00200-6.

[18] Ren F, Noda N-A. Adhesive strength evaluation for three-dimensional butt joint in terms of the intensity of singular stress field on the interface outer edge. Int J Adhesion Adhes 2019;98:102549. https://doi.org/10.1016/j.ijadhadh.2020.102549.

[19] Takaki R, Noda N-A, Ren F, Sano Y, Takase Y, Miyazaki T, et al. Variation of intensity of singular stress field (ISSF) along the interface outer edge of prismatic butt joint and debonding condition expressed by the ISSF. Int J Adhesion Adhes 2020;102:102665. https://doi.org/10.1016/j.ijadhadh.2020.102665.

[20] Labossiere PEW, Dunn ML. Fracture initiation at three-dimensional bimaterial interface corners. J Mech Phys Solids 2001;49(3):609–34. https://doi.org/ 10.1016/S0022-5096(00)00043-0.

[21] Benthem JP. State of stress at the vertex of crack in a half space. Int J Solids Struct 1977;13(5):479–92. https://doi.org/10.1016/0020-7683(77)90042-7.

[22] Benthem JP. The quarter-infinite crack in a half space; alternative and additional solutions. Int J Solids Struct 1980;16(2):119–30. https://doi.org/10.1016/ 0020-7683(80)90029-3.

[23] Bazant ZP, Estenssoro LF. Surface singularity and crack propagation. Int J Solids Struct 1979;15(5):405–26. https://doi.org/10.1016/0020-7683(79)90062-3.

[24] Takakuda K. Stress singularity at the crack tip of surface crack. Transactions of the Japan Society of Mechanical Engineers. Series A 1984;50(454):1193–2000. https://doi.org/10.1299/kikaia.50.1193. in Japanese.

[25] Takase Y, Noda N-A. SIF formula based on exact SIF distribution for semi-elliptical surface cracks subjected to mode I. II, III uniform, Fatigue Fract Eng Mater Struct 2024;47(5):1762–94. https://doi.org/10.1111/ffe.14239.

[26] Miyazaki T, Fujiwara T, Noda N-A, Sano Y. Three-dimensional singularity index at interface corner in prismatic butt joint under arbitrary material combination. Int J Solid Struct 2021;229(15):111120. https://doi.org/10.1016/j.ijsolstr.2021.111120.

[27] Wu Z. Experimental and numerical investigation of the interfacial strength of bi-material joints. Int J Adhesion Adhes 2017;77:29–34. https://doi.org/10.1016/ j.ijadhadh.2017.04.004.

[28] Hattori T., Sakata S., Hatsuda T., Murakami G., **1988**. A stress singularity parameter approach for evaluating adhesive strength. JSME international journal. Ser. 1, Solid mechanics, strength of materials, 31 (4), 718 – 723. https://doi.org/10.1299/jsmea1988.31.4_718.

[29] Iancu OT, Fett T, Munz DA. A fracture mechanical treatment of free edge stress singularities applied to a brazed ceramic/metal compound. Int J Fract 1990;46: 159–72. https://doi.org/10.1007/BF00017930.

[30] Amagai M. Investigation of stress singularity fields and stress intensity factors for cracks. Finite Elem Anal Des 1998;30(1):97–124. https://doi.org/10.1016/ S0168-874X(98)00034-1.

[31] Kitamura T, Shibutani T, Ueno T. Crack initiation at free edge of interface between thin films in advanced LSI. Eng Fract Mech 2002;69(12):1289–99. https:// doi.org/10.1016/S0013-7944(02)00009-7.

[32] Reedy Jr ED, Guess TR. Comparison of butt tensile strength data with interface corner stress intensity factor prediction. Int J Solids Structures 1993;30(21): 2929–36. https://doi.org/10.1016/0020-7683(93)90204-K.

[33] Qian ZQ, Akisanya AR. An investigation of the stress singularity near the free edge of scarf joints. Eur J Mech - A/Solids 1999;18(3):443–63. https://doi.org/ 10.1016/S0997-7538(99)00118-7.

[34] Imanaka M, Ishii K, Nakayama H. Evaluation of fatigue strength of adhesively bonded single and single step double lap joints based on stress singularity parameters. Eng Fract Mech 1999;62(4–5):409–24. https://doi.org/10.1016/S0013-7944(98)00111-8.

[35] Reedy Jr ED. Connection between interface corner and interfacial fracture analyses of an adhesively-bonded butt joint. Int J Solids Struct 2000;37(17):2429–42. https://doi.org/10.1016/S0020-7683(99)00002-5.

[36] Akisanya AR, Meng CS. Initiation of fracture at the interface corner of bi-material joints. J Mech Phys Solids 2003;51:27–46. https://doi.org/10.1016/S0022-5096(02)00076-5.

[37] Kitamura T, Hirakata H, Truong DV. Initiation of interface crack at free edge between thin films with weak stress singularity. Thin Sol Fi 2007;515(5):3005–10. https://doi.org/10.1016/j.tsf.2006.08.034.

[38] Afendi M, Teramoto T. Fracture toughness test of epoxy adhesive dissimilar joint with various adhesive thicknesses. J Solid Mech Mater Eng 2010;4(7): 999–1010. https://doi.org/10.1299/jmmp.4.999.

[39] Mintzas A, Nowell D. Validation of an H_{cr}-based fracture initiation criterion for adhesively bonded joints. Eng Fract Mech 2012;80:13–27. https://doi.org/ 10.1016/j.engfracmech.2011.09.020.

[40] Naito K, Onta M, Kogo Y. The effect of adhesive thickness on tensile and shear strength of polyimide adhesive. Int J Adhesion Adhes 2012;36:77–85. https://doi. org/10.1016/j.ijadhadh.2012.03.007.

[41] Takahashi Y, Aihara K, Ashida I, Higuchi K, Yamamoto Y, Arai S, et al. Evaluation of interfacial fracture strength in micro-components with different free-edge shape. Mech Eng J 2016;3(6):16–00108. https://doi.org/10.1299/mej.16-00108.

[42] Suzuki Y. Adhesive tensile strengths of scarf and butt joints of steel plates (Relation between adhesive layer thicknesses and adhesive strengths of joints. JSME Int J 1987;30(265):1042–51. https://doi.org/10.1299/jsme1987.30.1042.

[43] Noda N-A, Miyazaki T, Li R, Uchikoba T, Sano Y, Takase Y. Debonding strength evaluation in terms of the intensity of singular stress at the interface corner with and without fictitious crack. Int J Adhesion Adhes 2015;61:46–64. https://doi.org/10.1016/j.ijadhadh.2015.04.005.

[44] Miyazaki T, Noda N-A, Ren F, Wang Z, Sano Y, Iida K. Analysis of intensity of singular stress field for bonded cylinder and bonded pipe in comparison with bonded plate. Int J Adhesion Adhes 2017;77:118–37. https://doi.org/10.1016/j.ijadhadh.2017.03.019.

[45] Miyazaki T, Noda N-A. Evaluation of debonding strength of single lap joint by the intensity of singular stress field. J Phys Conf Ser 2017;842:012078. https://doi.org/10.1088/1742-6596/842/1/012078.

[46] Miyazaki T, Inoue T, Noda N-A, Sano Y. A precise and efficient method for evaluating singular stress field at the vertex in three dimensional bonded body. Trans JSME (in Japanese) 2018;81(864):18. https://doi.org/10.1299/transjsme.18-00013 [in Japanese].

[47] Noda N-A, Li R, Miyazaki T, Takaki R, Sano Y. Convenient adhesive strength evaluation method in terms of the intensity of singular stress field. Int J Comput Methods 2019;16(1):1850085. https://doi.org/10.1142/S0219876218500858.

[48] Koguchi H, Yokoyama K, Luangarpa C. Determination of the intensity of singularity at the vertex of interface in three-dimensional joints using a conservative integral (Effect of radius of integral domain and size of element). Trans JSME (in Japanese) 2016;82(833):15–00372. https://doi.org/10.1299/transjsme.15-00372 [in Japanese].

[49] Zhang Y, Noda N-A, Takahasi K-T, Lan X. Effect of adhesive thickness on the intensity of singular stress at the adhesive dissimilar joint. J Solid Mech Mater Eng 2010;4(10):1467–79. https://doi.org/10.1299/jmmp.4.1467.

[50] Zhang Y, Wu P, Duan M. A mesh-independent technique to evaluate stress singularities in adhesive joints. Int J Adhesion Adhes 2015;57:105–17. https://doi.org/10.1016/j.ijadhadh.2014.12.003.

[51] Zhang Y., Noda N. -A., Wu P., Duan M., **2015**. A mesh-independent technique to evaluate stress singularities in adhesive joints. Int J Adhesion Adhes, 57, 105 – 117 (The corrigendum of authorship is published in Int J Adhesion Adhes 60, 2015). https://doi.org/10.1016/j.ijadhadh.2014.12.003.

[52] Carpenter WC, Byers C. A path independent integral for computing stress intensities for V-notched cracks in a bi-material. Int J Fract 1978;35:245–68. https://doi.org/10.1007/BF00276356.

[53] Pageau SS, Joseph PF, Biggers SB, Jr,. The order of stress singularities for bonded and disbonded three-material junctions. Int J Solid Struct 1994;31(21):2979–97. https://doi.org/10.1016/0020-7683(94)90064-7.

[54] Pageau SS, Biggers SB, Jr.. Finite element evaluation of free-edge singular stress fields in anisotropic materials. Int J Numer Methods Eng 1995;38(13):2225–39. https://doi.org/10.1002/nme.1620381306.

[55] Koguchi H, Muramoto T. The order of stress singularity near the vertex in three-dimensional joints. Int J Solid Struct 2000;37(35):4737–62. https://doi.org/10.1016/S0020-7683(99)00159-6.

[56] Dundurs J. Discussion of edge-bonded dissimilar orthotropic elastic wedges under normal and shear loading. J Appl Mech 1969;36(6):650–2. https://doi.org/10.1115/1.3564739.

[57] Bogy DB. Edge-bonded dissimilar orthogonal elastic wedges under normal and shear loading. J Appl Mech 1968;35(3):460–6. https://doi.org/10.1115/1.3601236.

[58] Bogy DB. Two edge-bonded elastic wedges of different and wedge angles under surface tractions. J Appl Mech 1971;38(2):377–86. https://doi.org/10.1115/1.3408786.

[59] Herrera-Garrido MA, Mantič V, Barroso A. A powerful matrix formalism for stress singularities in anisotropic multi-material corners. Homogeneous (orthogonal) boundary and interface conditions. Theor Appl Fract Mech 2022;119:10327. https://doi.org/10.1016/j.tafmec.2022.103271.

[60] Herrera-Garrido MA, Mantič V, Barroso A. A semi-analytical matrix formalism for stress singularities in anisotropic multi-material corners with frictional boundary and interface conditions. Theor Appl Fract Mech 2024;129:104160. https://doi.org/10.1016/j.tafmec.2023.104160.

[61] Chen D. H. and Nisitani H., **1993**. Intensity of singular stress field near the interface edge point of a bonded strip. Transactions of the Japan Society of Mechanical Engineers, Series A, 59(567), 2682 - 2686 (in Japanese). https://doi.org/10.1299/kikaia.59.2682.

[62] Noda N-A, Shirao R, Li J, Sugimoto J-S. Intensity of singular stress fields causing interfacial debonding at the end of a fiber under pullout force and transverse tension. Int J Solid Struct 2007;44:4472–91. https://doi.org/10.1016/j.ijsolstr.2006.11.034.

[63] Takaki R, Noda N-A, Sano Y, Takase Y, Suzuki Y, Chao C-K. Fractographic identification of fracture origin mainly controlled by the intensity of singular stress field (ISSF) in prismatic butt joint with corner fillet. Int J Adhesion Adhes 2021;106:102810. https://doi.org/10.1016/j.ijadhadh.2021.102810.

[64] Sawa T, Ichikawa K, Shin Y, Kobayashi T. A three-dimensional finite element stress analysis and strength prediction of stepped-lap adhesive joints of dissimilar adherends subjected to bending moments. Int J Adhesion Adhes 2010;30(5):298–305. https://doi.org/10.1016/j.ijadhadh.2010.01.006.

[65] Noda N-A, Takaki R, Oda K, Suzuki Y. Variation of tensile adhesive strength prescribed by JIS depending on the adhesive geometries. in Japanese JSAE Transaction 2024;55(1):213–9. https://doi.org/10.11351/jsaeronbun.55.205.

[66] Nakano H, Sekiguchi Y, Sawa T. Three-dimensional FEM stress analysis and strength prediction of scarf adhesive joints with similar adherends subjected to static tensile loadings. in Japanese J Adhes Soc Japan 2013;49(3):82–91. https://doi.org/10.11618/adhesion.49.82.

[67] Nakano H, Omiya Y, Sekiguchi Y, Sawa T. FEM stress analysis and strength prediction of scarf adhesive joints with dissimilar adherends subjected to static tensile loadings. in Japanese J Adhes Soc Japan 2013;49(7):249–59. https://doi.org/10.11618/adhesion.49.249.

[68] Noda N-A, Takase Y. Generalized stress intensity factors of V-shaped notch in a round bar under torsion, tension, and bending. Eng Fract Mech 2003;70(11):1447–66. https://doi.org/10.1016/S0013-7944(02)00115-7.

[69] Lazzarin P, Filippi S. A generalized stress intensity factor to be applied to rounded V-shaped notches. Int J Solids Struct 2006;43(9):2461–78. https://doi.org/10.1016/j.ijsolstr.2005.03.007.

[70] Zappalorto M. Mode I Generalised Stress Intensity Factors for rounded notches in orthotropic plates. Theor Appl Fract Mec 2019;101:356–64. https://doi.org/10.1016/j.tafmec.2019.03.014.

[71] Chen D-H. Stress intensity factors for *V*-notched strip under tension or in-plane bending. Int J Fract 1994;70:81–97. https://doi.org/10.1007/BF00018137.

[72] Chen D-H, Nisitani H. Singular stress field near the corner of jointed dissimilar materials. J Appl Mech 1993;60(3):607–13. https://doi.org/10.1115/1.2900847.

[73] Noda N-A, Takase Y, Chen M. Generalized stress intensity factors in the interaction between two fibers in matrix. Int J Fract 2000;103:19–39. https://doi.org/10.1023/A:1007696723382.

[74] Oda K, Ashikari S, Noda N-A. Analysis method useful for calculating various interface stress intensity factors efficiently by using a proportional stress field of a single reference solution modeling. Arch Appl Mech 2024;94:779–800. https://doi.org/10.1007/s00419-024-02540-6.